To the Graduate Council:

I am submitting herewith a dissertation written by Kathleen Danyo Blackett, entitled "The Photoproduction of Possible Hybrid Mesons at $\langle E_\gamma \rangle = 110$ GeV." I have examined the final copy of this dissertation for form and content and recommend that it be accepted in partial fulfillment of the requirements for the degree of Doctor of Philosophy with a major in Physics.

George T. Condo, Major Professor

We have read this dissertation
and recommend its acceptance:

Accepted for the Graduate Council:

Associate Vice Chancellor and
Dean of the Graduate School

THE PHOTOPRODUCTION OF POSSIBLE HYBRID MESONS AT $\langle E_\gamma \rangle = 110$ GEV

A Dissertation

Presented for the

Doctor of Philosophy

Degree

The University of Tennessee, Knoxville

By

Kathleen Danyo Blackett

August 1995

This work is dedicated to my parents:
Roberta Marie Danyo
and
the late Mike William Danyo.

Acknowledgements

E687 is a tremendously successful effort, and I am greatly indebted to all of the members of the E687 collaboration. I cannot possibly mention all who have made significant contributions to the experiment, but I would like to at least mention a few. I am grateful to the spokesman of the experiment, Joel Butler, Jim Wiss and John Cumulat who were quite active during the course of the experiment and its analysis, and Paul Lebrun who took a special interest in the light quark mesons. I would also like to thank all those who designed and built the equipment, the PASS-1 er's, those who developed the Monte Carlo code and those who have contributed in other ways to numerous to mention. I especially thank all of those who were helpful to the UT group when we joined the collaboration.

Most of the analysis in this work was done on a Silicon Graphics 4D/240GTX Power Station operated by the UTKHEP group, although some analysis was performed via the Fermilab Computing System, the University of Tennessee Computing Center (UTCC), and a Hewlett-Packard Apollo Series 735s maintained by some members of the theoretical high energy physics group at UT. This manuscript was written in LaTeX, and data plots were made with the Physics Analysis Workstation (PAW). The diagrams were drawn either with the xfig package on most UNIX system or with the FeynDiag software by Bill Dimm.

Each member of my dissertation committee made a unique contribution, which is worth mentioning. I thank David Dobbs for graciously agreeing to participate on my committee even though he is not in the physics department. I thank Ted Barnes whose advice and counsel led to significant improvements in this work. I thank Bill

Bugg; he has provided me with a research assistantship funded by the Department of Energy (DOE) contract DE-AS05-76ERO3956 and the Science Alliance. I thank Tom Handler who is the UT group leader on E687, and is responsible for UT's participation on the experiment. Most of all, I thank my advisor, George Condo, whose candid advice and insights into physics greatly contributed to this work. It has been a pleasure to work for him.

My time spent in Tennessee would not have been the same without the women of the UT Women's Rugby Football Club. I thank them for their friendship and support over the last few years.

For their love, support, and many trips to Tennessee I would like to thank my family: my mom, Roberta Danyo, my sisters, Beth Danyo and Nancy Cuddihy, and my brother, Michael Danyo. They will all be happy to know that I am now looking for a job.

Lastly and most importantly I thank my husband, Gavin Blackett, for his advice and patience throughout the compilation of this dissertation. He has dragged me kicking and screaming through the computational world – not an easy task. He has read the roughest of the rough drafts, and still has found time to do the wash and walk the dog. He is a wonderful husband and an excellent physicist.

Abstract

The search for exotic resonances is one of the most active areas in light meson spectroscopy at the present time. From a study of high energy photoproduction on experiment E687 at Fermi National Accelerator Laboratory, two candidates for hybrid states are observed.

The first is a state with a decay into $f_1(1285)\pi$ which has a mass of 1748 ± 12 MeV and a width of 136 ± 30 MeV, whose decay angular distributions suggest the true exotic quantum numbers $J^{PC} = 1^{-+}$.

The second is a state of mass 1914 ± 33 MeV and width 389 ± 115 MeV, produced with almost no background, which decays to $\phi\eta$ and whose angular distributions indicate $J^{PC} = 1^{--}$. Close and Page predict the existence of a hybrid vector meson that decays to $\phi\eta$. However their theoretical width is much less than our experimental value.

Contents

List of Tables

List of Figures

Chapter 1

Introduction

One of the specialties of the University of Tennessee (UT) high energy physics group is light meson spectroscopy. Since the light quark mesons have been studied for decades, a great deal is known about them. However there is much about them which is still unknown. One of the aspects in the light meson sector which needs further elaboration is that of gluonic degrees of freedom.

There are several theories for bound states including gluons, and there are several candidate states for them, but so far, their existence remains uncertain. One particular class of these states, the so-called hybrid states, should be accessible by experiment according to some models. Two possible hybrid states, one of which decays into $f_1(1285)\pi$ and the other which decays into $\phi\eta$, will be analyzed at length in this dissertation.

Chapter 2

Theory

2.1 The Vector Meson Dominance Model

Meson photoproduction is the process whereby photons interact inelastically with matter to produce mesons. The experimental observation, that these interactions are dominated by the production of vector mesons, is incorporated into the vector meson dominance (VMD) model. The underlying principle of VMD is that the photon manifests itself as a virtual (off the mass shell) vector meson, provided it has sufficient energy to produce the vector meson [1]. Hence the photon can be described as a superposition of a bare, or structureless, component and a hadronic component. The photon wave function is given by:

$$|\gamma\rangle \cong \sqrt{Z_3}|\gamma_{bare}\rangle + c\sqrt{\alpha}|h\rangle$$

where $Z_3 = 1 - c^2\alpha$ assures the proper normalization, α is the fine structure constant, and c is a constant of $O(1)$. It is assumed in VMD that the bare component of the photon $|\gamma_B\rangle$ cannot interact with hadrons. In its simplest formulation, VMD asserts that the vector mesons ρ^0, ω and ϕ are the sole hadronic constituents of the photon, based on the observation of their copious photoproduction [2]. These vector mesons have the same quantum numbers as the photon, $J^{PC} = 1^{--}$ with $Q = S = 0$. Here J is the total spin of the meson, P is the parity, C is the

charge conjugation, Q is its electric charge and S is the strangeness. Photoproduction of the vector mesons is predominantly due to diffractive processes (Pomeron exchange), which have been found to conserve s-channel helicity.

2.2 The Standard Model

The elementary particles are categorized in the standard model, which is the most widely accepted theory of elementary particles at the present time. According to the standard model, all matter is composed of fermions (spin $\frac{1}{2}$ particles) called quarks and leptons. Quarks and leptons also have antimatter counterparts [1] - antiquarks and antileptons - which behave similarly but have opposite electric charges and magnetic moments.

Leptons can be charged, such as the e, μ, or τ, or they can be neutral, such as the neutrinos ν_e, ν_μ, or ν_τ, which have very little or no mass. Leptons exist individually, but quarks must exist in groups called hadrons. There are six types or "flavors" of quarks, *up, down, strange, charm, bottom* and the recently discovered *top* whose symbols are *u, d, s, c, b* and *t* respectively. Hadrons can be baryons (antibaryons), which are composed of three quarks (antiquarks), or mesons, which are composed of a quark and an antiquark. The masses of the quarks and leptons are given in Table 1. Although values for the quark masses are listed, these are somewhat uncertain due to the fact that they cannot be determined directly; they must be determined by their influence on hadronic properties.

The behavior of quarks and leptons is governed by force carriers called gauge bosons (integer spin particles). A list of the fundamental forces and their corresponding gauge bosons is given in Table 2. The strong force, characteristic of hadrons, is mediated by gluons. Photons are carriers of the electromagnetic force, and the W and Z vector bosons are carriers of the weak force. The electromagnetic and the weak force are unified at very high energies and are often collectively

[1] Antiquarks and antineutrinos are denoted with a bar over them, such as $\bar{u}$ and $\bar{\nu}_\mu$.

Table 1: Generations of quarks and leptons.

Generation	Quarks			Leptons		
		Mass (MeV)	Charge		Mass (MeV)	Charge
I	u	$2-8$	$+2/3$	e	0.511	-1
	d	$5-15$	$-1/3$	ν_e	0	0
II	s	$100-300$	$-1/3$	μ	105.7	-1
	c	~ 1500	$+2/3$	ν_μ	0	0
III	b	$4100-4500$	$-1/3$	τ	1777	-1
	t	~ 174000	$+2/3$	ν_τ	0	0

Table 2: The fundamental forces and their corresponding gauge bosons.

Force	Gauge Bosons
Strong Force	g
Weak Force	Z^0, $W^\pm$
Electromagnetic Force	γ
Gravity	graviton

referred to as the electroweak force. The body of knowledge concerning the electromagnetic force is known as quantum electrodynamics (QED), while quantum chromodynamics (QCD) describes phenomena involving the strong force. A spin 2 graviton is presumed to carry the gravitational force, but has not yet been observed experimentally.

2.3 The Quark Model

The quark model, which is an attempt to reproduce experimental results, describes the quark content of hadrons. Because this dissertation is devoted to meson photoproduction, no further discussion of baryons will be given.

If the quark content of the light mesons is plotted with the strangeness, S (related to the number of s quarks), on the y-axis and the isospin, I (related to the number of u and d quarks), on the x-axis, a pattern emerges due to the $SU(3)$ flavor symmetry. This pattern is shown in Figure 1. The quark model can be expanded to $SU(4)$, $SU(5)$ and $SU(6)$ symmetries with the addition of the c, b and t quarks respectively. $SU(3)$ is an approximate symmetry because the mass of the s quark is slightly greater than that of the u and d quarks. If the heavier quarks are included, the accuracy of the model is further degraded. However, the $SU(3)$ flavor symmetry is appropriate for the light quark states since the effective masses of the u, d and s are quite close. Hence for states composed of the light quarks, the quark model gives an accurate description of them.

In $SU(3)$ flavor symmetry, the quark and the antiquark are $\mathbf{3}$ and $\bar{\mathbf{3}}$-dimensional objects respectively. The coupling of a quark (q) and an antiquark ($\bar{q}$) can be expressed as the following:

$$\mathbf{3} \otimes \bar{\mathbf{3}} = \mathbf{8} \oplus \mathbf{1}.$$

The result is an octet and a singlet, collectively referred to as a nonet, for each J^{PC}. The quark representations of the mesons with $J^{PC} = 0^{-+}$ and $J^{PC} = 1^{--}$ are listed in Table 3 [3]. It should be noted that the quark content of the neutral states in the

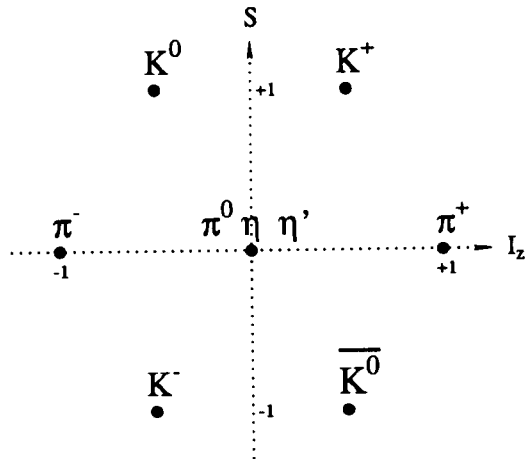

a) J=0

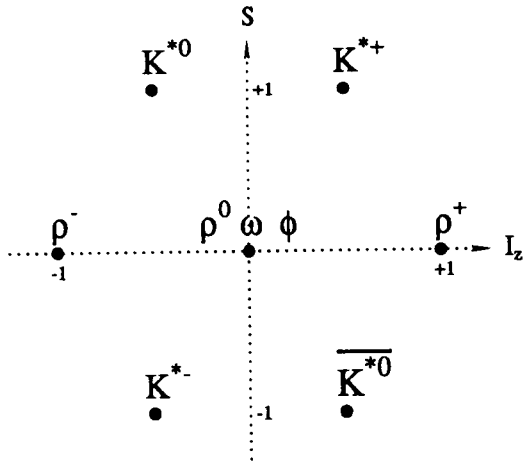

b) J=1

Figure 1: (a) $J = 0$ nonet and (b) $J = 1$ nonet.

Table 3: Quark representations of mesons.

J=0	J=1	Charge	Quark Content
π^+	ρ^+	$+1$	$u\bar{d}$
π^-	ρ^-	-1	$d\bar{u}$
π^0	ρ^0		$u\bar{u}$
η	ω	0	$d\bar{d}$
η'	ϕ		$s\bar{s}$
K^+	K^{*+}	$+1$	$u\bar{s}$
K^0	K^{*0}	0	$d\bar{s}$
K^-	K^{*-}	-1	$s\bar{u}$
$\overline{K^0}$	$\overline{K^{*0}}$	0	$s\bar{d}$

center of the nonets is not precisely delineated. Due to $SU(3)$ symmetry breaking, states with the same IJ^P and additive quantum numbers can mix. Therefore the $I = 0$, or isoscalar, member of an octet can mix with the corresponding singlet. The $I = 1$, or isovector, member cannot have any strange quark content since s and $\bar{s}$ have $I = 0$. The isovector can be expressed:

$$\pi^0 = (d\bar{d} - u\bar{u})/\sqrt{2}.$$

Physically only mixed states are observed for the isoscalars. Mixing is quite prominent in the ground state nonet, where the physical states η and η' are expressed in terms of a mixing angle, ϕ:

$$|\eta\rangle = \cos\phi|ns\rangle - \sin\phi|s\bar{s}\rangle$$
$$|\eta'\rangle = \sin\phi|ns\rangle + \cos\phi|s\bar{s}\rangle$$

where

$$|ns\rangle = (u\bar{u} + d\bar{d})/\sqrt{2}.$$

In strong interactions isospin (I), parity (P), charge conjugation (C) and G-parity (G) are all conserved quantities. C is not an eigenstate of charged mesons, but G-parity, which combines C and I, *is* a useful quantum number for *both* charged and neutral states. G-parity can be expressed as $G = C_n(-)^I$, where C_n is the charge conjugation of the corresponding neutral state. In the quark model, parity, P, and charge conjugation, C, for mesons are expressed as $P = (-)^{L+1}$ and $C = (-)^{L+S}$ respectively, where L is the orbital angular momentum between the $q\bar{q}$ pair, and S is their spin (either 0 or 1 for mesons). It is apparent that in the quark model certain quantum numbers are forbidden. These forbidden quantum numbers, $J^{PC} = 0^{--}, 0^{+-}, 1^{-+}, 2^{+-}$ and so on, are also referred to as *exotic* combinations of quantum numbers. A list of the allowed states using spectroscopic notation ($^{2S+1}L_J$) is given in Table 4 [4].

2.4 Color and Confinement

Both quarks and gluons possess an internal degree of freedom called color. Color is required to avoid violations of the Pauli Exclusion Principle in the quark model. An elementary example of this is the Δ^{++} baryon whose quark model assignment is (uuu). With three quarks of the same flavor, an additional degree of freedom (color) must be introduced. Color charge is somewhat analogous to electric charge, except the gluon carries color charge while the photon does not carry electric charge. Therefore, unlike photons, gluons couple directly to themselves.

Three color charges form the members of the $SU(3)$ symmetry group, independent of the $SU(3)$ flavor symmetry of the light quarks. Quarks can have a color charge of red (r), green (g), or blue (b), and similarly antiquarks can have color charges of antired ($\bar{r}$), antigreen ($\bar{g}$) or antiblue ($\bar{b}$). Quarks and antiquarks are $\mathbf{3}$ and $\bar{\mathbf{3}}$-dimensional objects respectively in the $SU(3)$ color group. Only color neutral states of hadrons can exist, such as $q\bar{q}$ (consisting of a quark with some color charge and an antiquark with the corresponding anticolor charge) and qqq

Table 4: Allowed $q\bar{q}$ states.

	PC_n			
J	$-+$	$+-$	$--$	$++$
0	$^1S_0$			$^3P_0$
1		$^1P_1$	$^3S_1, ^3D_1$	$^3P_1$
2	$^1D_2$		$^3D_2$	$^3P_2, ^3F_2$
3		$^1F_3$	$^3D_3, ^3G_3$	$^3F_3$
4	$^1G_4$		$^3G_4$	$^3H_4, ^3F_4$

(consisting of one quark of each color). States which cannot form a color singlet such as $qq\bar{q}$, qq and q are forbidden. This phenomenon is often referred to as confinement in QCD.

The gluons form a color octet analogous to the flavor octet of the light mesons. Thus the gluons are 8-dimensional objects in the $SU(3)$ color group. The gluonic states can be written as the following [5]:

$$r\bar{b}, r\bar{g}, b\bar{g}, b\bar{r}, g\bar{r}, g\bar{b}, \frac{r\bar{r}-b\bar{b}}{\sqrt{2}}, \frac{r\bar{r}+b\bar{b}-2g\bar{g}}{\sqrt{6}}.$$

A diagram of the color force being mediated between a quarks and an antiquark by the exchange of a single gluon is shown in Figure 2. However because of gluon self-coupling, the simple diagram in Figure 2 gives an accurate description of violent collisions involving high momentum transfer, but is less important than many-gluon processes of low momentum transfer (large distances). The potential between a quark and an antiquark in a color singlet can be modeled by

$$V_S = -\frac{4}{3}\frac{\alpha_s}{r} + kr.$$

The first term, which dominates at small r, is due to their Coulombic attraction and is the contribution from single gluon exchange. The linear term is associated with confinement at large r.

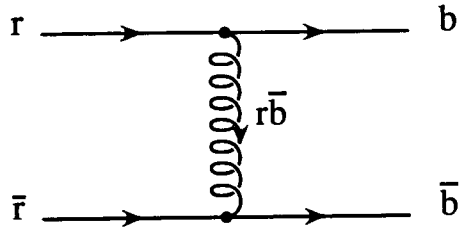

Figure 2: The exchange of a single gluon between a quark and an antiquark.

This phenomenon is illustrated by the fact that as a quark and an antiquark are separated, the force (and also the number of field lines) between them increases, and they form a string or flux tube as pictured in Figure 3. If enough potential energy is added and pair production is allowed, it becomes energetically favorable for the system to become two mesons with short flux tubes rather than one meson with a long flux tube.

2.5 Exotics

At the present time, there has been no unambiguous proof of the existence of exotic states [2]. A compelling signature for the existence of one of these states would be the observation of a state with forbidden, or exotic J^{PC} quantum numbers. Two groups of these predicted states are multiquark states and gluonic hadrons. States with gluonic degrees of freedom are categorized as either glueballs or hybrids.

Glueballs are states without quark content which consist entirely of gluons. Models for low-lying glueballs can be found in references [6] and [7]. From an experimental point of view, the determination of a glueball will be difficult because their decay widths are uncertain most models predict the glueballs with exotic quantum numbers to have masses which are quite large.

[2]States outside of the $q\bar{q}$ quark model are referred to as *exotic*. However, not all of the states predicted outside of the quark model have exotic J^{PC} quantum numbers; but if a state *does* have exotic J^{PC} quantum numbers, it *must* be outside of the quark model.

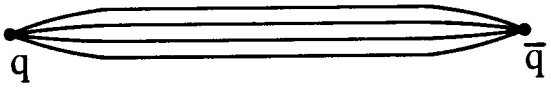

Figure 3: Mesonic structure including the flux tube.

Hybrids are $q\bar{q}$ pairs combined with a gluonic excitation. Experimentally, a search for hybrids is more attractive than one for glueballs since certain characteristic decays of hybrids are expected, and all hybrid models predict some states with exotic quantum numbers. In particular, all hybrid models predict a state with $J^{PC} = 1^{-+}$ [8]. Theoretical studies of hybrid states include the MIT bag model [9, 10, 11], techniques with QCD sum rules [12, 13], and models with constituent gluons [14, 15, 16]. Currently one of the most widely used models to study hybrids is the flux tube model, which will be discussed in the following section.

2.5.1 The Flux Tube Model

The flux tube model proposed by N. Isgur *et. al.* [17] predicts masses and widths of a variety of hybrid mesons with exotic and non-exotic quantum numbers. Confirming one of these states would demonstrate the existence of states beyond the quark model. The credibility of the flux tube model is enhanced by the fact that it accurately describes the well established $q\bar{q}$ mesons [18]. In this model a meson consists of a $q\bar{q}$ pair joined by the flux tube. The flux tube was first described as a cylindrical bag of colored fields, and later modeled as a string of mass points with a confining potential between them [19]. The flux tube is in the ground state for conventional mesons, and it is in an excited state for hybrid mesons. A glueball in this model is an excited flux tube in a continuous loop. Diagrams of the creation and decay of both an ordinary and hybrid meson are shown in Figure 4.

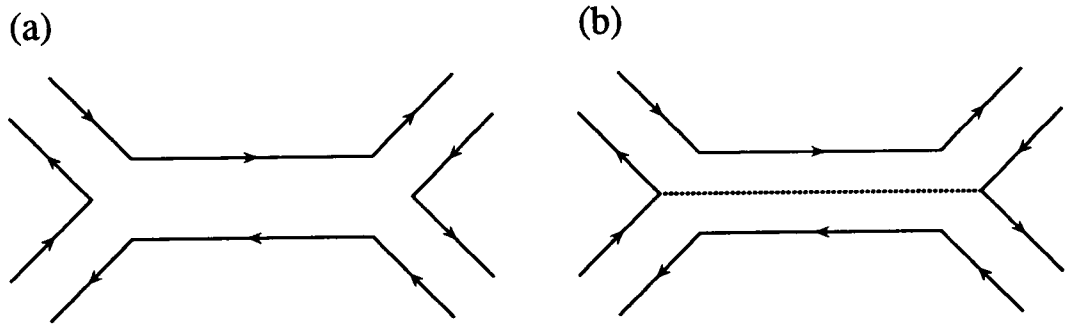

Figure 4: Feynman diagrams of the creation and decay of (a) an ordinary meson and (b) a hybrid meson, where the gluonic excitation is represented by a dotted line.

According to the flux tube model, final states consisting of two ground state mesons, such as those of the π and ρ nonets, are highly suppressed because the rotational wave function of the excited string cannot be easily absorbed by them. This model predicts that the lowest-lying hybrid mesons preferentially decay into final states with one orbitally excited meson, such as $b_1(1235)\pi$, $f_1(1285)\pi$, $h_1(1170)\pi$ or $a_1(1260)\pi$. Unfortunately many of these flux tube hybrids are predicted to have widths which are far too wide to observe experimentally, or they are predicted to decay to states whose widths are so large that their own identification is usually somewhat uncertain. However, a 1^{-+} state with a mass of about 1900 MeV and a width of about 180 MeV is predicted by this model to decay into $b_1(1235)\pi$ and $f_1(1285)\pi$. The flux tube model is relevant to this work because a feature of this model is that photoproduction appears to be an ideal source for the creation of flux tube model hybrid mesons [17, 20]. Furthermore, the $f_1(1285)\pi$ is readily available in this experiment.

2.5.2 Experimental Evidence for Flux Tube Model Predictions

The most recent published work in the search for this state is by J. H. Lee *et. al.* at Brookhaven National Laboratory (BNL) [21] using the reaction $\pi^- p \rightarrow \overline{K}_S K^+ \pi^- \pi^- p$. This group has analyzed the $f_1(1285)\pi$ state where the $f_1(1285)$ decays to $a_0(980)^+\pi^-$ and the $a_0(980)^+$ subsequently decays to $\overline{K}_S K^+$. They report the existence of both a $J^{PC} = 1^{++}$ resonance at 1700 MeV and a $J^{PC} = 1^{-+}$ partial wave extending from 1600 to 2200 MeV in the $f_1(1285)\pi$ mass spectrum. If this latter wave corresponds to resonance production, this experiment heralds the experimental observation of an exotic state, perhaps a hybrid. Because of the importance of this result, it is highly desirable to confirm it independently by observing it in a different reaction. Although the production mechanism was expected to be $b_1(1235)$ exchange, the actual data showed it to be either ρ or $f_2(1270)$ exchange. A diagram for this process is located in Figure 5(a).

The $f_1(1285)\pi$ channel is analyzed in this work where the data are produced via photoproduction instead of with a π beam. This process is diagrammed in Figure 5(b). If VMD and one pion exchange (OPE) are assumed in these data, the interaction vertex in E687 is identical to that in the experiment of Lee *et. al.*

The $b_1(1235)\pi$ final state has been analyzed in two previous photoproduction experiments. T. Handler *et. al.* [22] report two primary mass enhancements in the $b_1(1235)^{\pm}\pi^{\mp}$ channel. The first, of mass 1672 ± 8 MeV, is consistent with the $\omega_3(1670)$ which is listed by the Particle Data Group as having $\omega\pi\pi$ and possibly $b_1(1235)\pi$ decay modes. The second enhancement with a mass of 1946 ± 25 MeV, occurs in a region where a hybrid is expected. M. Atkinson *et. al.* [23] also report the observation of the ω_3 in this channel, along with an additional mass enhancement at 1880 ± 40 MeV. Although both experiments are highly suggestive of the existence of a $b_1(1235)\pi$ state at $\sim$ 1900 MeV, neither experiment contained sufficient statistics to quantify its J^{PC}.

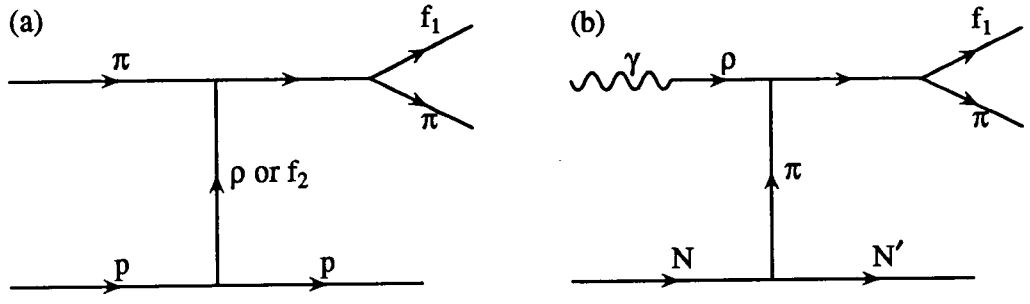

Figure 5: Production mechanism for $f_1(1285)\pi$ at (a) BNL and (b) FNAL.

F. E. Close and P. R. Page [24] predict that there may be a significant contribution from the $\rho\pi$ channel to the decay of the proposed exotic states in the flux tube model. A state at 1775 MeV with a large $\rho\pi$ decay width has been observed in a photoproduction bubble chamber experiment at SLAC [25]. The most likely quantum number assignment for this state was $J^{PC} = 1^{-+}$, although certain non-exotic combinations could not be excluded.

Close and Page [24] also extend predictions of the flux tube model to hybrid states with non-exotic quantum numbers. Proof that states with non-exotic quantum numbers correspond to hybrid states will be more difficult to obtain. Two such states have a substantial decay to the $\phi\eta$ final state, which will be analyzed in this dissertation. The $\phi\eta$ decay modes, representing $s\bar{s}$ hybrid states, are predicted to evolve from a $J^{PC} = 1^{+-}$ resonance and a $J^{PC} = 1^{--}$ resonance. Because of the similarity of the quantum numbers to those of the photon, diffractive production of this state is a distinct possibility. Both of these $\phi\eta$ resonances are also predicted to decay to $\phi\eta'$ and K^*K as well as various other excited K combinations. However these channels are not analyzed due to the large amount of background from competing processes.

$\phi\eta$ is an exciting channel from an experimental point of view. First of all, previous investigations of the $\phi\eta$ system have been quite limited. The Particle Data Group reports $\phi\eta$ to be one of the many decay modes of the J/ψ, but it is

not listed as a decay mode for any of the light quark meson resonances. Secondly, the ϕ and the η are both quite narrow and occur near their respective thresholds in channels representing large decay fractions, which facilitates the analysis of the $\phi\eta$ system.

Chapter 3

E687 Beamline and Spectrometer

The analyses in this work are based on data from the fixed target experiment E687 carried out at Fermi National Accelerator Laboratory (FNAL) in Batavia, Illinois. A schematic of Fermilab [26] is given in Figure 6. The experiment ran periodically between 1987 and 1992. Data for this analysis was accumulated between 1990 and 1992, during which time over 500 million triggered events were recorded. The following chapter is a condensed description of the beamline and the spectrometer. An unabridged version is available in references [27] and [28].

3.1 Beamline

3.1.1 Proton Beamline

The proton beam originates as negatively ionized hydrogen which is accelerated to an energy of 0.75 MeV in the Cockcroft-Walton voltage multiplier, and then further accelerated by the LINAC to an energy of 200 MeV where it also passes through a carbon foil and the electrons are stripped off [29]. From the LINAC, protons are injected into the booster, which is a small proton synchrotron accelerator 75 meters in diameter. After being accelerated in the booster ring, the protons enter the main ring, which is two kilometers in diameter and accelerates the protons to

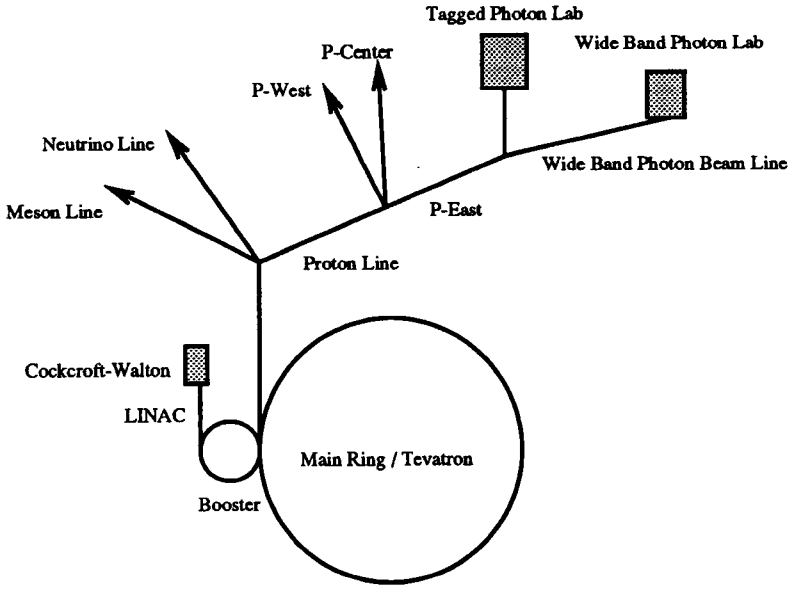

Figure 6: Schematic layout of Fermi National Accelerator Laboratory.

energies of 150 GeV. Finally, from the main ring, the protons are injected into the Tevatron, which is the superconducting accelerator located just below the main ring. Here the protons are accelerated to their highest energy – 800 GeV.

Once this energy is reached the beam then goes to a switchyard where it is split electrostatically for the fixed target experiments into three beamlines – the meson line, the neutrino line, and the proton line. E687 is located in Wide Band Hall at the end of the wide band photon beamline beyond P-East.

3.1.2 The Photon Beamline

At a proton accelerator, photons must be derived indirectly from strong interactions. Two problems arise: first, the beam must be formed from particles produced over a wide range of momenta and angles, and second, all unwanted particles produced with the photons must be removed. The wide band photon beam derived here is called a tertiary beam because it emerges from three interactions and a

decay. Although this somewhat degrades the final energy, it is an extremely pure beam. (Neutral hadronic contamination is less than 10^{-5} per photon.)

A schematic of the derivation of the photon beam can be found in Figure 7. The process was carried out in the following manner:

- The 800 GeV protons interact with the *primary production target*, which consists of liquid deuterium. Dipole magnets subsequently sweep away the charged particles into a mass of concrete which acts as a dump, and the neutral particles, mainly neutrons, K_L's and photons, continue downstream.

- The neutral particles then strike a lead converter with a thickness of 0.5 radiation lengths. This particular radiation length was chosen so that the photons would be likely convert to e^+e^- pairs, but the other neutral particles would be unlikely to interact hadronically.

- The electrons are bent away from the forward direction by a beam transport system consisting of dipole and quadrupole magnets. Any remaining neutral particles continue forward into a neutral dump. The electron momenta is tagged with a silicon strip detector, and only electrons within $\pm 15\%$ of a nominal momentum of 350 GeV continue down the beamline.

- The electrons then strike a lead radiator of 0.2 radiation lengths where photons are produced by bremsstrahlung ($e^- + Z \rightarrow e^- + Z + \gamma$). Afterwards the electrons are swept aside by dipole magnets, and their momenta are determined by the Recoil Electron Shower Calorimeter (RESH). The photons continue forward to the experimental target.

3.1.3 Beam Tagging

The incident photon energy was determined on an event-by-event basis according to the relation

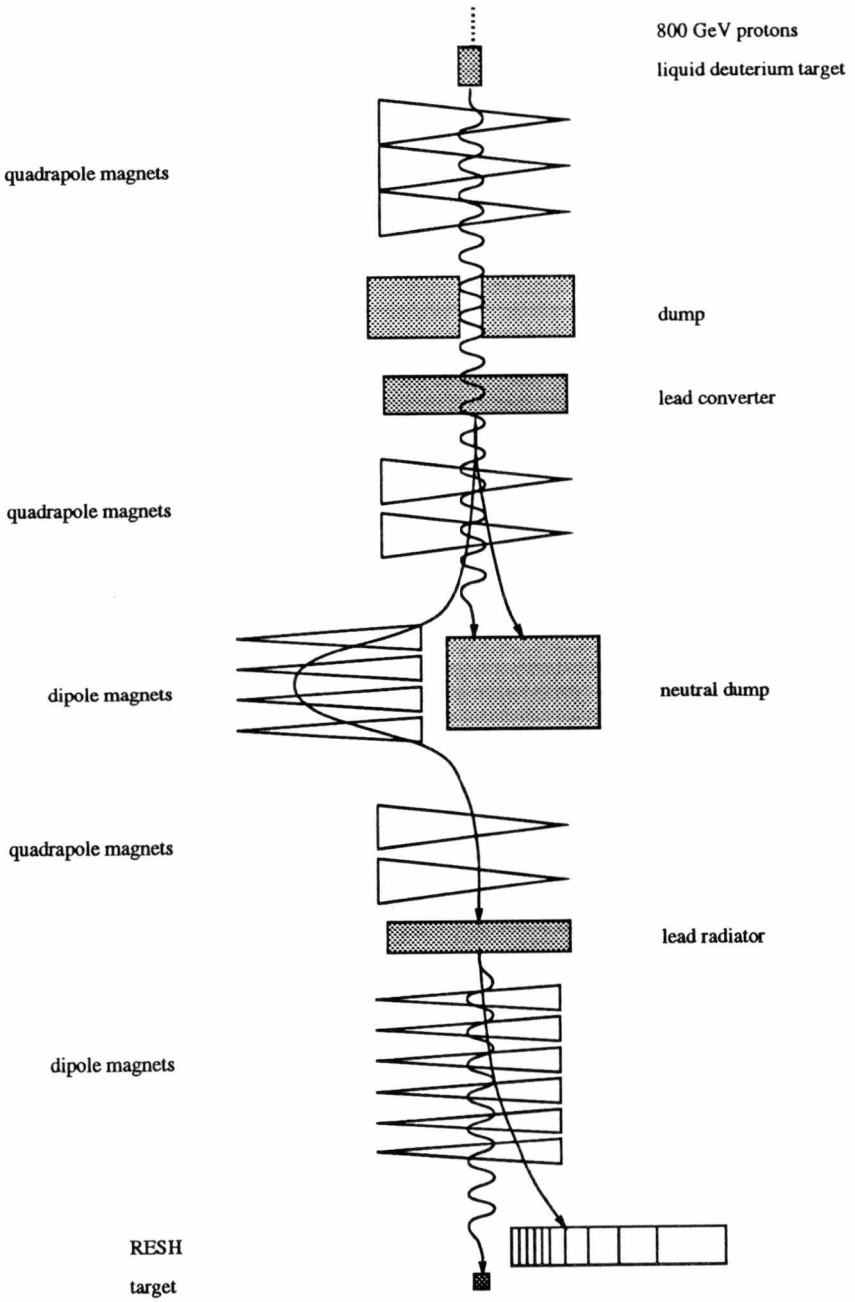

Figure 7: Schematic of formation of tertiary bremsstrahlung photon beam.

$$E_\gamma = E_{e^-}^{beam} - E_{e^-}^{recoil} - E_{\gamma'}.$$

- $E_{e^-}^{beam}$ is the electron energy determined by the silicon strip beam tagging detector. This detector consists of five large area microstrip planes – one in between the dipole magnets, two upstream from the dipole magnets and two downstream. They were placed as far apart as possible to obtain the best resolution of the bend angle. The middle plane was used to delineate multiple beam tracks, spurious noise, and out of time hits. A schematic of this detector planes is shown in Figure 8 [30].

- $E_{e^-}^{recoil}$ is the energy measured by the RESH. The RESH consists of 10 scintillator hodoscope counters transverse to the photon beam, as shown in Figure 9 [31]. The particular counter struck determines the bend angle of the electron which in turn determines its momentum. The electrons which do not undergo bremsstrahlung in the radiator are deflected 10.24 centimeters from the beamline into a lead/steel dump.

- $E_{\gamma'}$ is the energy due to non-interacting photons and the photons produced in multiple bremsstrahlung processes. These photons were measured by the Beam Gamma Monitor (BGM) in the 1990 run and by the Beam Calorimeter (BCAL) in the 1991 run. These electromagnetic calorimeters are located at the end of the spectrometer. They are also sensitive to e^+e^- pairs.

3.2 The Spectrometer

The E687 spectrometer [28] is a highly efficient, large acceptance, multiparticle spectrometer capable of operating at high rates. Although it was primarily designed for the detection of charm particles, it can yield information on many light quark processes as well. A schematic of the spectrometer can be found in Figure 10, and a rendered drawing of the spectrometer can be found in Figure 11 [30].

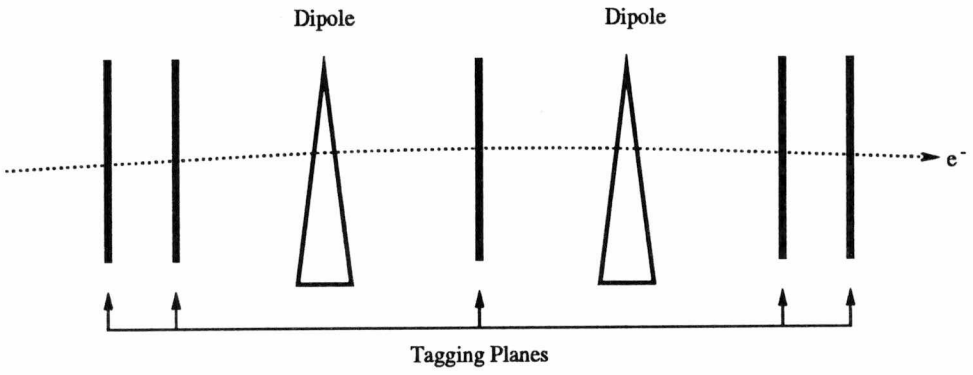

Figure 8: Configuration of tagging planes for the e^- beam.

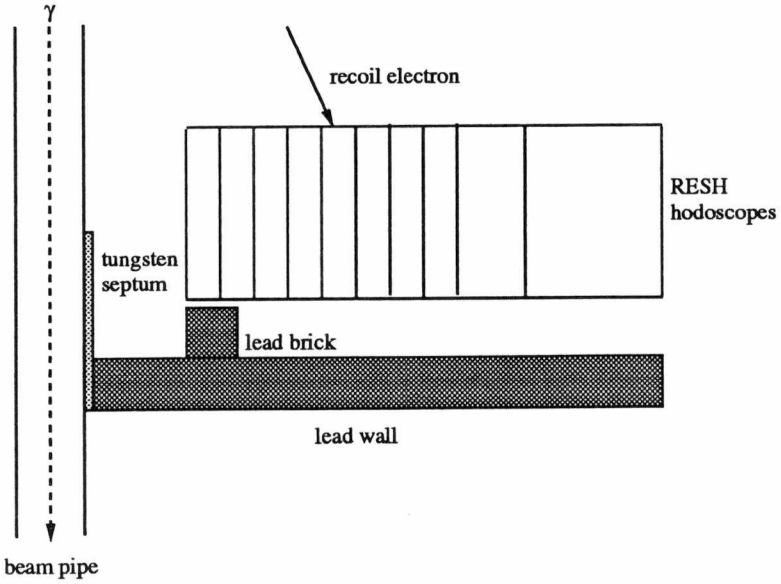

Figure 9: Configuration for the Recoil Electron Shower Calorimeter (RESH).

(a)

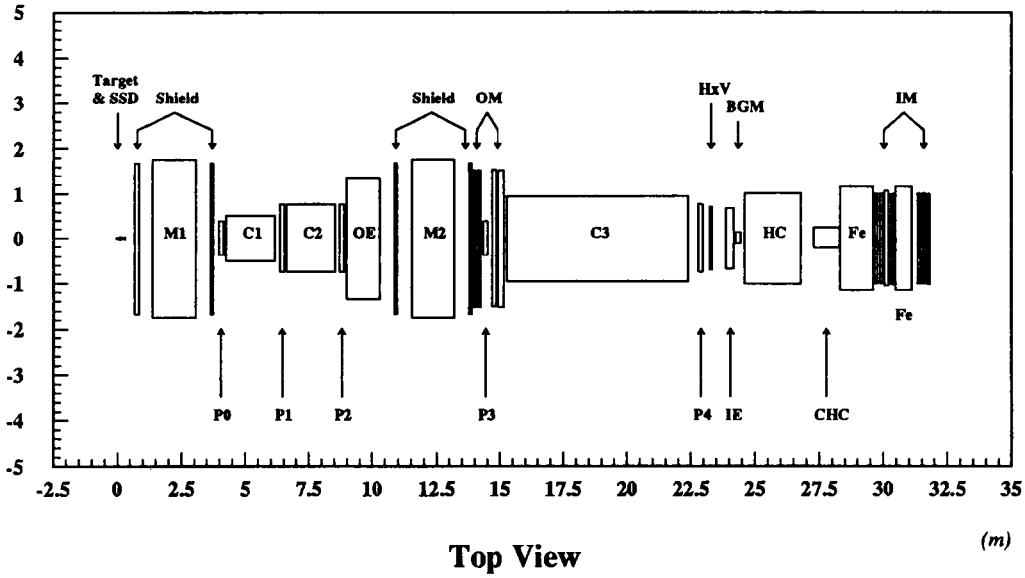

Top View

(b)

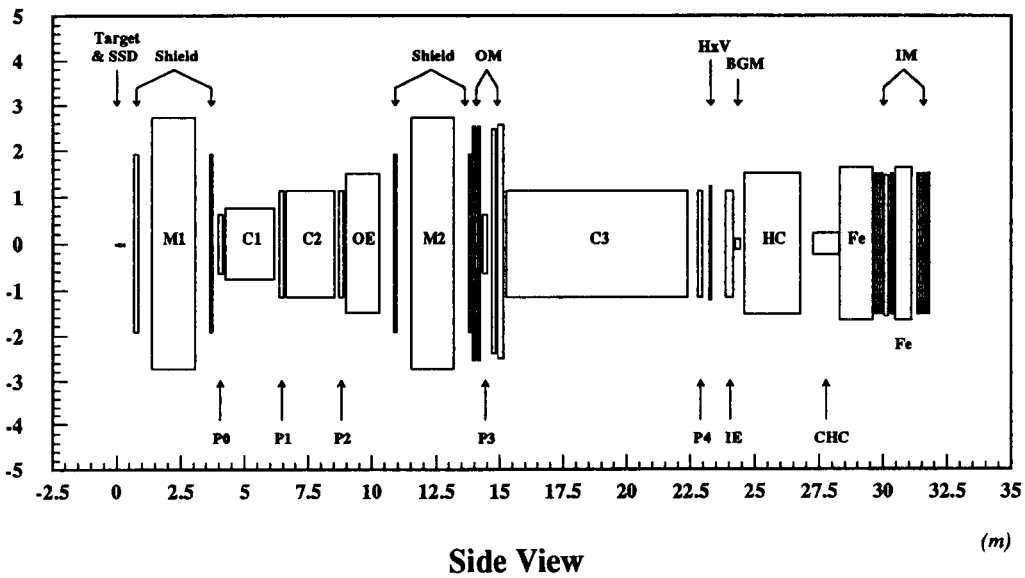

Side View

Figure 10: Schematic of the Spectrometer.

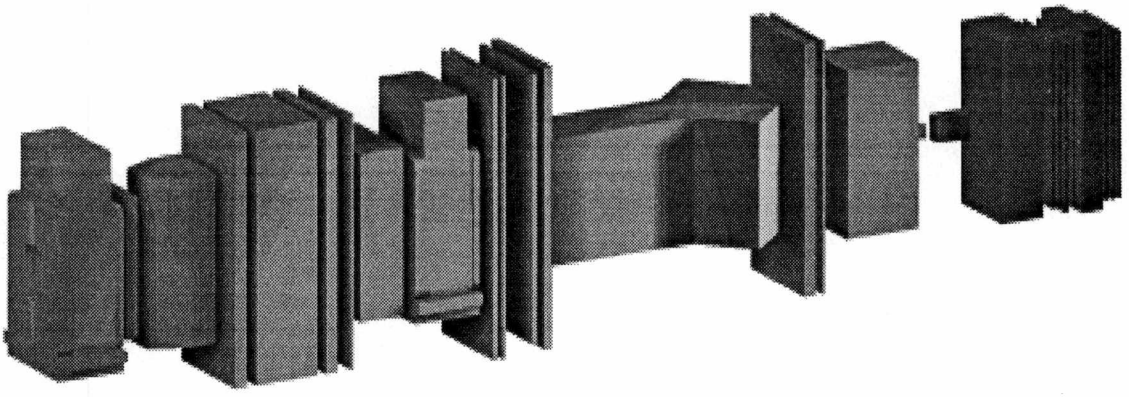

Figure 11: The E687 Spectrometer.

3.2.1 The Target

Although several targets were used during the course of the experiment, the data in this analysis were taken with a beryllium target in place. Because hadronic cross sections are proportional to A (the atomic number of the material), and e^+e^- cross sections are proportional to Z^2 (the atomic mass squared), beryllium was a preferred target since it has a small Z^2/A ratio.

3.2.2 Silicon Microstrip Detectors

The silicon microstrip detector is located 7 cm downstream from the target. It consists of 12 planes grouped into 4 stations of 3 detectors each, as shown in Figure 12 [32]. The detectors at each station measure signals in the i, j and k directions, which are oriented $-135°$, $-45°$ and $-90°$ to the horizontal x-axis of the spectrometer reference frame respectively. The first station and the innermost regions of the other stations have twice the resolution as the remaining parts. The overall detection efficiency is over 99% for each plane - even after accounting for non-functional strips and defective electronic channels. High resolution tracking is extremely important in this device for discerning heavy flavor decay vertices from the primary interaction vertex.

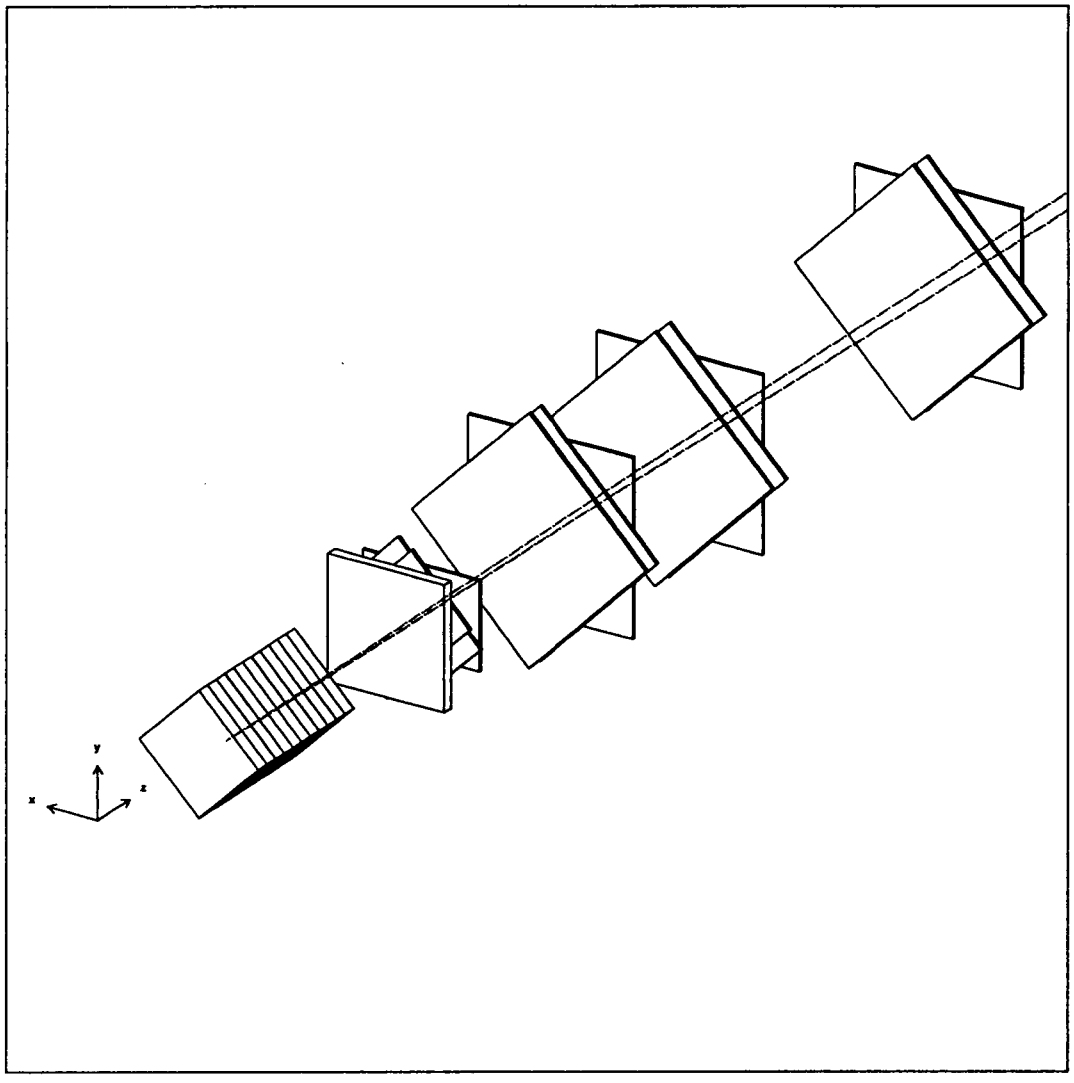

Figure 12: The target and silicon strip detector.

3.3 Analyzing Magnets

Momenta of charged tracks are determined by means of two large aperture dipole magnets, M1 and M2. A drawing of these magnets is shown in Figure 13 [30], and their specifications are listed in Table 5. The ratio of the p_t kicks of M1 and M2 was chosen so that charged tracks return to their original undeflected position toward the downstream end of the spectrometer.

The arrangement of the magnets was primarily chosen to reduce the e^+e^- background, which travels almost parallel to the beam. M1 separates the pair as it travels through its aperture. Slower pairs usually strike either the pole tips of M1 or the face or pole tips of M2. Pairs with enough forward momentum are bent back toward the beam axis by M2. The beam profile is reconstructed at the end of the spectrometer, where there is a small amount of imprecision due to the energy loss from any bremsstrahlung which may occur. Most hadronic events will have at least two particles outside the pair region at the downstream end of the spectrometer.

3.3.1 Proportional Wire Chambers

Charged particle tracking is accomplished by means of the five proportional wire chambers (PWC's). Three of them (P0 - P2) are located between M1 and M2, and the other two (P3 and P4) are located after M2. This arrangement allows for two independent momentum measurements for tracks which travel as far as P3.

Each chamber consisted of four planes of wire in four different directions, X, Y, U and V. X and Y measure the track position in the horizontal and vertical directions, while U and V are oriented ± 11.3 degrees with the horizontal axis. Although the X and Y planes alone would be sufficient, the U and V planes are key to reducing track reconstruction ambiguity. A diagram of the wire orientations is given in Figure 14. The chambers are filled with a 65/35 argon-ethane gas mixture bubbled through ethyl alcohol at 0 degrees Celsius and are operated at voltages

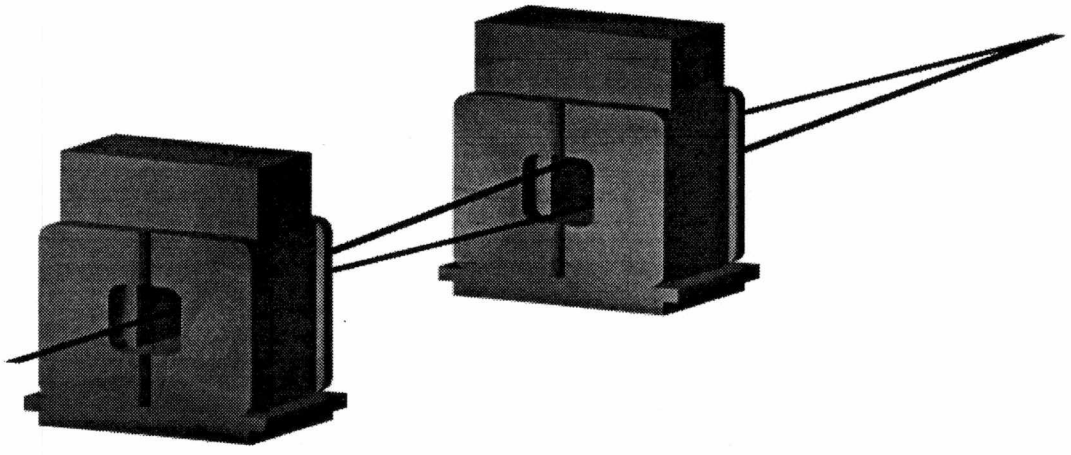

Figure 13: The analyzing magnets.

Table 5: Specifications of Analyzing Magnets.

Magnet	Current (A)	p_t (GeV)
M1	1020	0.400
M2	2000	0.850

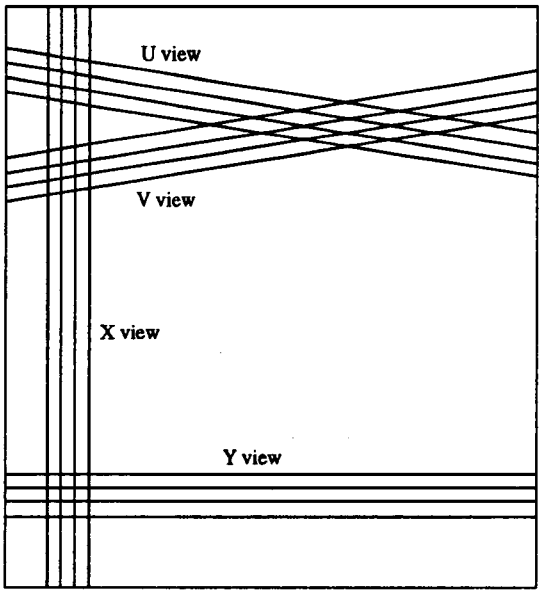

Figure 14: Schematic of wire arrangement.

between 2.8 and 3.5 kV.

3.3.2 Čerenkov Counters

The purpose of the Čerenkov counters is to identify charged particles. There are three such counters in the spectrometer, C1, C2 and C3, each filled with gas at atmospheric pressure. These counters operate on the principle that a charged particle traversing some medium will emit a conical wave front of photons if its velocity exceeds the velocity of light in that medium. Thus, light is emitted in a Čerenkov counter if

$$\beta = \frac{P}{E} \geq \frac{1}{n},$$

where n is the index of refraction of the gas in the counter. The threshold momentum needed for a charged particle traversing a Čerenkov counter to fire a cell can

be expressed:

$$P_{threshold} = \frac{M}{\sqrt{n^2 - 1}}.$$

The emitted light is focused via mirrors onto phototubes. The arrangement of the mirrors inside C1 is shown in Figure 15 [33]. The gases were chosen so that there is a wide range of momentum values in which pions, kaons, and protons could be identified. Particular momentum ranges for a given mass produce unique combinations of the individual counters, and hence particle identification is accomplished. Specifications of the Čerenkov counters are listed in Table 6.

3.3.3 Muon Detectors

Muon detection is accomplished by means of the Inner Muon detector (IM) and the Outer Muon detector (OM). Both utilize planes of scintillator hodoscopes and proportional tubes to detect minimum ionizing particles. See Table 7. The muon system is described in greater detail in references [34] and [35].

The IM is located between M1 and M2. It consists of a 121 cm steel filter (about 10 interaction lengths), two planes of proportional tubes, two planes of scintillating hodoscopes, a 60 cm steel muon filter, two more planes of proportional tubes, and one more plane of hodoscopes.

The OM is located directly after M2. It is similar to the IM except it has a hole through the center to match that of the M2, and the iron yoke of the M2 (approximately 10 interaction lengths) doubles as a muon filter for the OM.

3.3.4 Hadron Calorimetry

Hadron calorimetry is implemented by means of two devices, the main Hadron Calorimeter (HC) and the Central Hadron Calorimeter (CHC). These calorimeters cover only the inner portion of the spectrometer. Their purpose is to select hadronic events as part of the energy trigger by recording energy from the hadronic showers. For approximately 34% of the run, events were selected when at least 40 GeV was

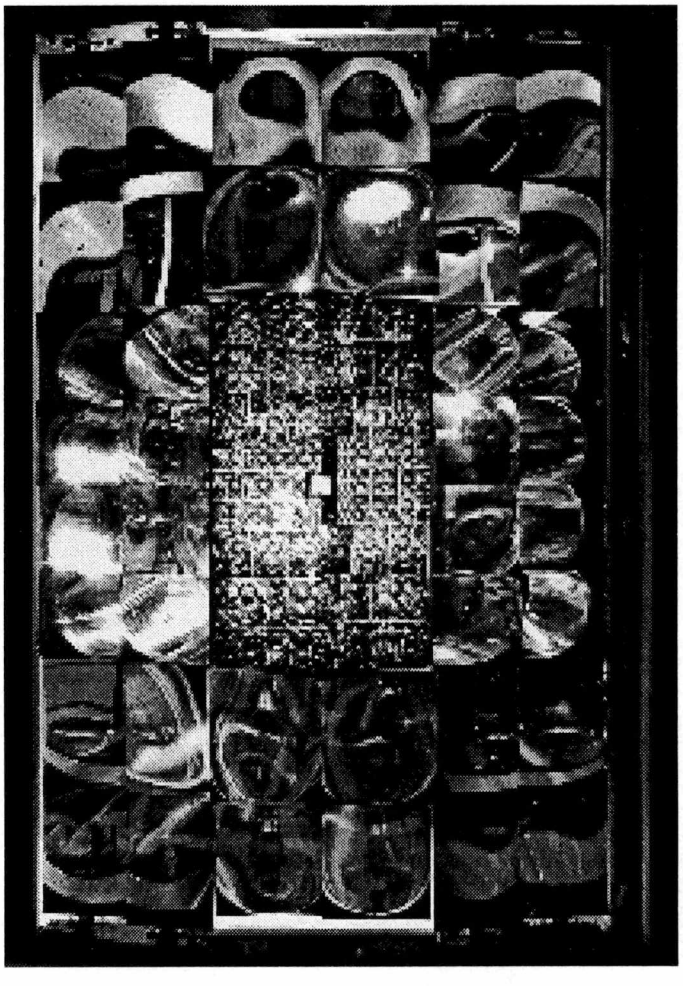

Figure 15: Mirrors inside C1.

Table 6: Specifications of Čerenkov Counters.

Counter	Gas	Threshold Momentum (GeV)			Number of Cells
		pions	kaons	protons	
C1	He and N_2	6.7	23.3	44.3	90
C2	N_2	4.5	16.2	30.9	110
C3	He	17.0	61.0	116.2	100

Table 7: Muon Detector Planes.

Detector	Plane	Function
IM	IM1X	Proportional tubes
	IM1Y	Proportional tubes
	IM1H	Scintillating Hodoscopes
	IM1V	Scintillating Hodoscopes
	IM2X	Proportional tubes
	IM2Y	Proportional tubes
	IM2H	Scintillating Hodoscopes
OM	OMX	Proportional tubes
	OMY	Proportional tubes
	OMH	Scintillating Hodoscopes

deposited. For the remainder of the run this selection criterion was raised to 50 GeV [36]. This requirement effectively rejects purely electromagnetic interactions.

The HC is a steel/gas sampling calorimeter with a tower readout geometry. It consists of 28 steel planes in alternation with 28 layers of sense planes. Each sense plane consists of a concentric pattern of pads filled with a 50/50 argon-ethane gas mixture for detecting ionization from showering particles. The signal from each tower is split by a fanout circuit. One line is fed to an ADC and integrated for 800 ns, while the other forms the hadronic energy trigger [37].

The CHC, which covered the hole in the HC during the 1990 part of the run, is of importance because it recorded the hadronic energy deposited in the region with the highest density of tracks. It was located between the HC and the first muon filter. Photons and e^+e^- pairs were absorbed in the BGM, so only hadrons showered in the CHC. In 1991 the BGM and the CHC were replaced with a new CHC with a hole through the center so that the photon beam could reach E683, a new experiment directly downstream from E687. The new CHC allowed the beam to pass but still measured the off-axis hadronic energy [34].

3.3.5 Electromagnetic Calorimetry

Electromagnetic calorimetry is carried out in the Inner Electromagnetic Calorimeter (IE) and the Outer Electromagnetic Calorimeter (OE). Detailed descriptions of the IE and OE are given in references [36] and [38]. These devices aid in distinguishing $e^{\pm}$'s from $\pi^{\pm}$'s and in reconstructing π^0's.

The OE is located just before M2. It consists of five alternating layers of lead, aluminum, and plastic scintillator. It has a large central aperture (51 cm $\times$ 88 cm), and a gap along the y-axis to keep e^+e^- pairs from beam photon conversions from showering in the calorimeter.

The IE, located between P4 and the HC, consists of 100 sheets of lead in alternation with 100 planes of circular scintillating fibers. An absorber was placed in the IE for the second half of the 1991 run.

Chapter 4

Data Acquisition and Reconstruction

4.1 Triggering

Because of the large number of e^+e^- pairs produced in E687, a very efficient triggering system is required to prevent overwhelming the Data Acquisition System (DAQ). (In E687, $\gamma Be \rightarrow e^+e^- : \gamma Be \rightarrow hadrons$ is about 500:1 [36].) The triggering system of E687 is a two level process consisting of the *Master Gate* and the *Second Level Trigger*. Its aim is to reject purely electromagnetic events while keeping hadronic events.

4.1.1 Master Gate

The first level trigger, called the *Master Gate* is the primary "filter" for purely electromagnetic events. It is designed to detect two or more charged tracks while rejecting e^+e^- pairs. It also requires that the event be created by a photon in the target rather than charged contaminant particles. The Master Gate is a *logical* device which utilizes signals from several counters located in the beamline and the spectrometer. Figure 16 illustrates a schematic of the Master Gate counters, which

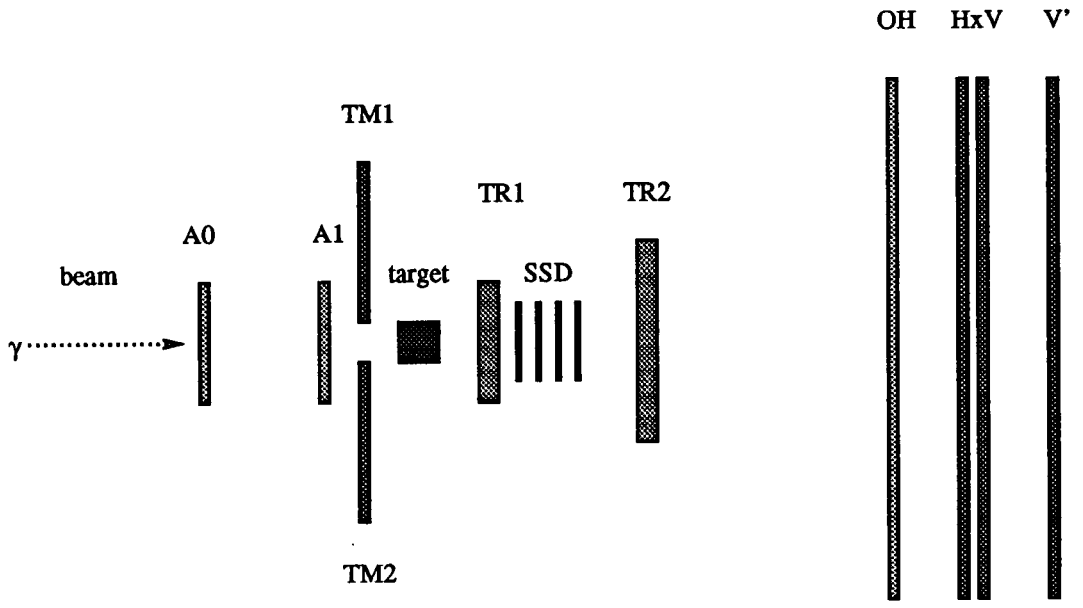

Figure 16: Schematic of the triggering system for the Mater Gate. (Not to scale.)

are described as follows:

- **A0 and A1** are scintillator counters placed in the beamline and are located approximately five meters and two meters upstream from the target respectively. A signal in either of these indicate a charged particle in the beam.
- **TM1 and TM2** are two counters located between A1 and the target. Their purpose is to veto muons in the diffuse muon halo which runs parallel to the beam.
- **TR1 and TR2** are scintillators located directly in front of the first station of microstrip planes and directly behind the last station of microstrip planes. These counters ensure that the photon successfully interacts in the target by detecting only singly ionized charged particles exiting the target region. Coincidence of TR1 and TR2 is required for the Master Gate trigger.

- **OH, H $\times$ V, and V$'$** together cover the entire acceptance region of the spectrometer. The OH, located between P2 and the OE, detects wide angle tracks that do not go through the aperture in M2. The H$\times$V, located just downstream from P4, detects the presence of one or more charged tracks outside the pair region. V$'$ was added behind the IE during the 1991 run to improve the efficiency of the detector. Both *inner-outer* and *outer-outer* logic is encorporated in the Master Gate. *Inner-outer* corresponded to coincidence hits between OH and H$\times$V and is denoted $OH \cdot (H \times V)_{1body}$. *Outer-outer* corresponds to two hits in the $H \times V$ and is denoted $(H \times V)_{2body}$.

Several Master Gates were used during the run. They are as follows [34].

$$MG = TR1 \cdot TR2 \cdot (H \times V)_{2body} \cdot \overline{(A0 + A1)}$$

and

$$MG = (TR1 \cdot TR2) \cdot \{(H \times V)_{2body} + OH \cdot (H \times V)_{1body}\} \cdot \overline{(A0 + A1)}$$

were used in the 1990 run. These Master Gates were also used in the 1991 run in addition to

$$MG = (TR1 \cdot TR2) \cdot \{(H \times V)_{2body} + OH \cdot (H \times V)_{1body}\} \cdot \overline{(A0 + A1 + TM1 + TM2)}$$

and

$$MG = (TR1 \cdot TR2) \cdot \{(H \times V')_{2body} + OH \cdot (H \times V')_{1body}\} \cdot \overline{(A0 \cdot A1)}.$$

4.1.2 Second Level Trigger

If events are accepted by the Master Gate, they are then passed on to the *Second Level Trigger*. The Master Gate has a dead time of about 2.4 μs, during which the Second Level decisions are made. Information from the slower detectors is latched by the Master Gate and used in the Second Level Trigger, where signals from the detectors are combined logically and can be adjusted to specific desired combinations. The Energy Trigger, which was used predominantly throughout the experiment, logically combines the following requirements:

- A minimum amount of hadronic energy.
- A minimum amount of RESH energy.
- At least one hit outside of the central pair region in P0.

If the Second Level Trigger is not satisfied, a fast clear is issued and the DAQ is reset and readied for a new Master Gate event [39].

4.2 Data Acquisition System

A diagram of the Data Acquisition System (DAQ) [39] is shown in Figure 17. The DAQ incorporates the following steps:

- After the beam hits the target, a signal is sent from the spectrometer to the counting room where most of the electronics reside.
- A Master Gate is then generated and the signals are recorded by ADC's, TDC's and latches.
- The Second Level Trigger decides whether to keep the event. If the Second Level Trigger is not generated, the event is cleared. If all is well, the data are read out into four Fastbus buffers while further Master Gates are inhibited. Once the signals are in the buffers, the electronics are cleared for the next event.
- From the buffers, data are read out to tape by "PANDA", a specialized data acquisition system, which concatenates and writes the data to 8 mm tapes [40].
- Several Sun and DEC stations ran on-line software via a UNIX hoist. This allows a verification of the data in real time.

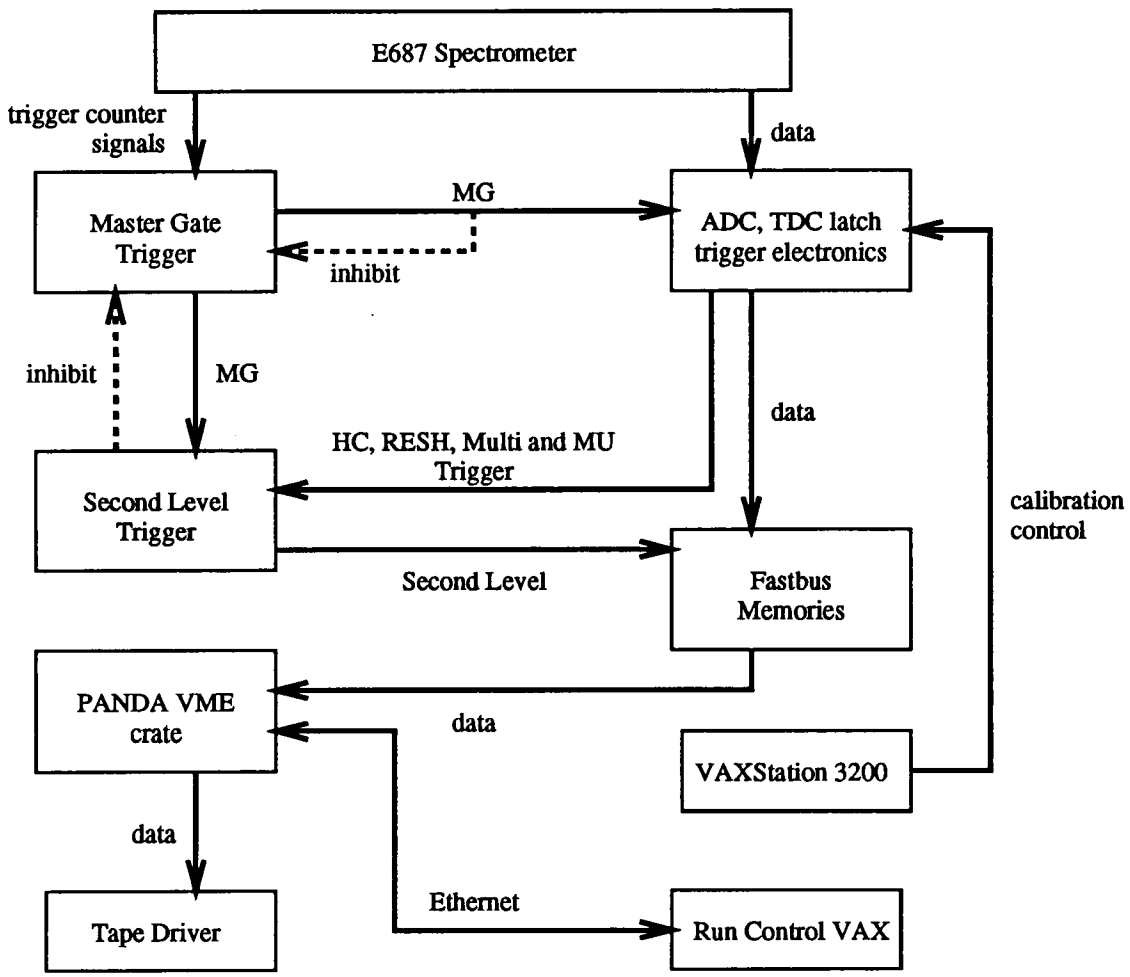

Figure 17: Schematic of the Data Acquisition System.

4.3 Reconstruction

After the data are taken, the raw data tapes are processed on IBM and SGI computer farms at Fermilab where the data are reconstructed via the PASS1 algorithms. The PASS1 reconstruction routines produce Čerenkov particle information, locate electromagnetic and hadronic showers in the calorimeters, and incorporate TDC, ADC, and latch information to reconstruct charged tracks. Each reconstruction task is performed by separate algorithms described in this section. The blocks of reconstructed data are then written to 8 mm magnetic tapes. The reconstruction algorithms are discussed in greater detail in reference [28].

4.3.1 Track Reconstruction

Pattern recognition algorithms are employed to deduce tracks. Tracks are reconstructed in the SSD and the PWC's separately, and then a *linking* algorithm is used to match the corresponding tracks. Tracks are put into four categories:

- *"5-Chamber" tracks* are those which go through M2. There is also a small group of tracks that go through M2, but not the last PWC plane.
- *"Stubs"* or *"3-chamber" tracks* are either wide angle or low momentum tracks which pass through P0 - P2.
- *"Unlinked SSD Tracks"* are either low momentum or wide angle tracks which failed to traverse M1.
- *"Tracks from decays downstream of P0"* can be either kinks or vee's. Kinks are due to a charged particle decaying to another charged particle and a neutral particle, and vee's are due to a neutral particle decaying into two charged particles.

The tracking is executed by the following algorithms:

SSD Tracks

First, analyses of clusters of adjacent hits are implemented to ensure that the number of crossing particles is consistent with the amount of charge released for each cluster. Then the SSD tracks are derived by an algorithm which fits the hits in the different SSD planes to a straight line via the least squares method in the three separate views. The algorithm allows an angular alignment error of no more than 6.0×10^{-5} radians between stations. The algorithm also requires a projection to have at least three of the four possible hits per view. Tracks sharing one of two projections are arbitrated on the basis of their χ^2 value. Hits not associated with any reconstructed track are used to search for wide angle tracks and for single segments of tracks caused by light multiple Coulomb scattering. The transverse resolutions are given by

$$\sigma_x = 11\mu m \sqrt{1 + \left(\frac{17.5 \text{ GeV}}{p}\right)^2}$$

$$\sigma_y = 7.7\mu m \sqrt{1 + \left(\frac{25 \text{ GeV}}{p}\right)^2}$$

where $11\mu m$ and $7.7\mu m$ are the contributions due to granularity, and the expressions in the radicals are due to multiple Coulomb scattering.

PWC Tracking

The algorithm used here considers projections in all four views of the PWC's: the U, V, and Y views which are distorted by M1 and M2 and the X view which is unaffected by the magnets. The algorithm initially uses the X view hits and a seed generated by the SSD algorithm. Then, projections from all four views are combined to form tracks. Further X projections are constructed from hits which have not been already used. These are then matched with unused hits in the U, V, and Y projections to construct additional tracks. A χ^2 per degree of freedom cut

is applied to each track. Tracks are required to have hits in P0 and in at least two other PWC chambers. Tracks could have at most 4 missing hits and no more than two missing hits in a single chamber. There is also additional arbitration between tracks with shared projections and various magnetic corrections.

Ancillary routines accounted for low momentum or wide-angle tracks which are often missed. In these routines the microstrip tracks are extended to predict hits in P0, P1 and P2. These tracks are only considered valid if the deviation from actual X hits is less than two wire spacings.

Linking

After the SSD and PWC tracks are established they need to be *linked.* The linking algorithm compares the extrapolated positions of the SSD tracks and the PWC tracks at the center of M1. If they match within a certain tolerance they are refit using all SSD and PWC information. A maximum of two PWC hits are allowed to be linked to the same microstrip track. This would occur in the instance of an e^+e^- pair which often appears as a single track in the SSD.

4.3.2 Neutral Vee Reconstruction

K^0_s, Λ^0 and their respective antiparticles are commonly called the neutral vee particles. For their reconstruction, pairs of oppositely charged tracks which have a high probability of forming a vertex are sought. In the reconstruction of a K^0_s, which decays to $\pi^+\pi^-$, tracks are assigned π masses to form an invariant mass. Similarly, in the case of the Λ^0, tracks are assigned π and p masses to form an invariant mass. The neutral vees can be divided into three categories: target region vees, M1 region vees and reconstruction vees. Plots of the reconstructed $\pi^+\pi^-$ mass spectra are shown in Figures 18 and 19 [36].

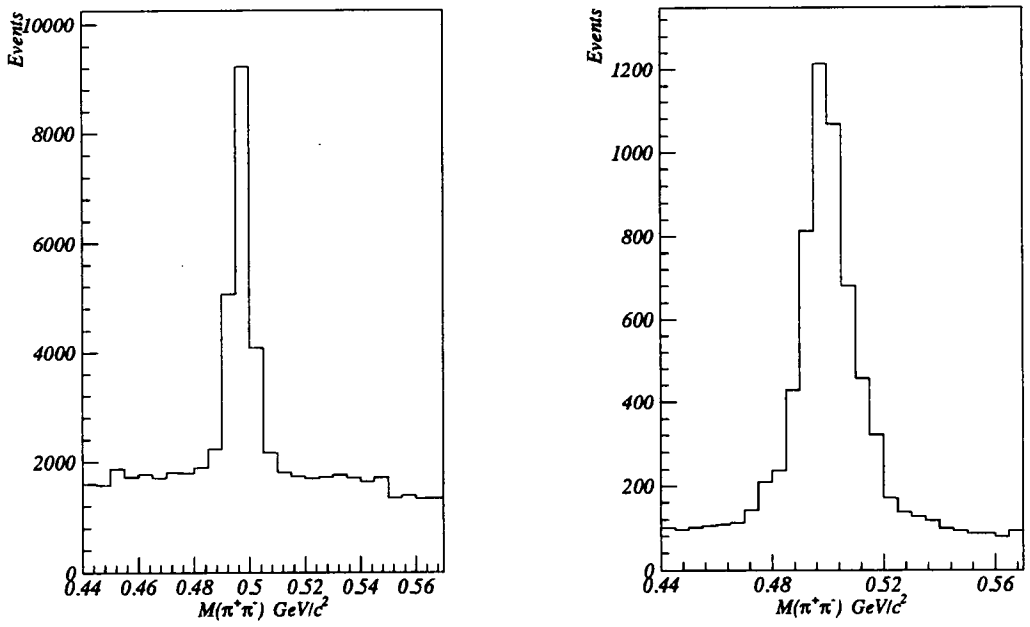

Figure 18: K_S peaks reconstructed from $\pi^+\pi^-$ pairs for (a) SSD vees and (b) reconstruction vees.

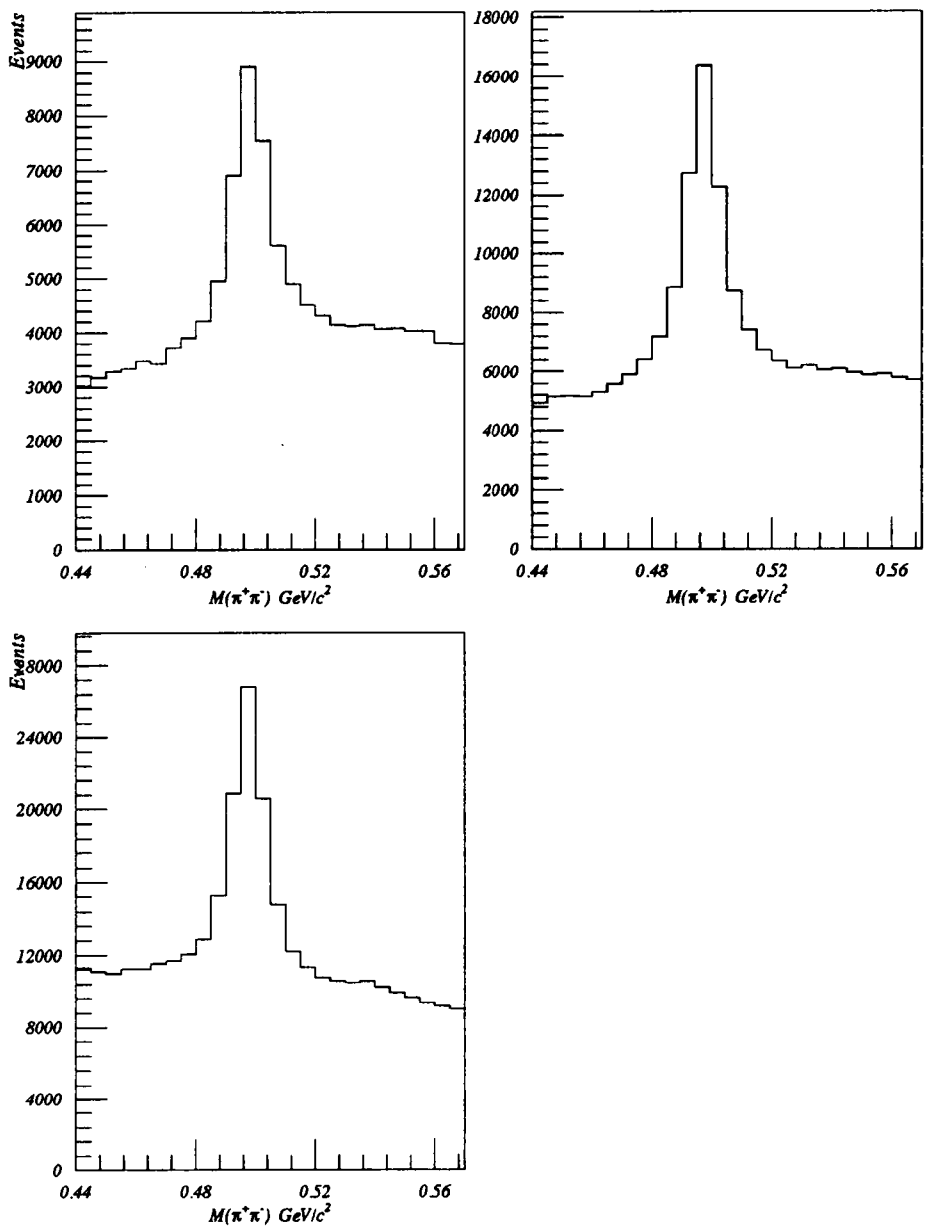

Figure 19: K_S peaks reconstructed from $\pi^+\pi^-$ pairs in the M1 region for (a) "Track-Track" vees, (b) "Track-Stub" vees and (c) "Stub-Stub" vees.

Target Region Vees

The target region vees are divided into two subcategories, *SSD Vees*, which decay upstream of the microstrips, and *MIC Vees*, which decay in the microvertex detector.

For the case of SSD vees, algorithms loop over all pairs of oppositely charged microstrip tracks linked to PWC tracks and fit them to determine a vertex. Cuts are employed to reduce the combinatorial background. The vee vertex is required to be at least 20 σ_L from the primary vertex, where σ_L is the error on the distance between the primary and vee vertices. The vee vector (the sum of the momentum vectors of the daughter particles) is required to extrapolate within 1 mm of the primary vertex in the transverse direction.

In the case of *MIC Vees*, an MIC algorithm extrapolates PWC tracks into the fourth or most downstream microstrip station. "Triplets", are formed from unused hits in the fourth station. If a triplet is found, the track parameters are recalculated and the track is projected upstream to the next microstrip station, where the search for triplets is continued. Arbitration among triplets is based on the χ^2 global fit to all hits associated with a given track. All combinations of oppositely charged tracks are tested for their distance of closest approach which eliminates most of the spurious tracks. Finally a loose mass cut is applied to K_s and Λ candidates.

M1 Region Vees

The M1 region, defined by the area between the last microstrip plane and P0, is the most densely populated of the vee regions. All vees in this region are reconstructed using PWC tracks. These vees fall into three categories.

- *"Track-Track"* vees are formed by two unlinked 5-chamber tracks
- *"Track-Stub"* vees are formed by one 5-chamber track and one 3-chamber track.

- *"Stub-Stub"* vees are formed by two 3-chamber tracks.

The algorithm consists of a routine that estimates the location of the vee vertex in the xz plane followed by an iterative procedure which determines the y coordinate of the vertex and the momentum of all of the non-5-chamber tracks. The vee is required to point back to the primary vertex as in the case of the target region vees.

Reconstruction Vees

Reconstruction vees are those which decay in the region between P0 and P2. Only hits not used in the PWC tracks are used here. Since the reconstruction vee decay region is field free, no magnetic trace is required to locate them. This algorithm begins with a search for single track projections in the X view. Then track hits are matched with the U, V, and Y to form track candidates. Single track fits are performed with a loose χ^2 cut on each. Tracks of opposite charge are paired together, and those with an acceptable fit are sent to an arbitration algorithm which ensures that no X-projection is used in more than one vee.

Vees which decay between P1 and P2 and those whose decay tracks exited the spectrometer before passing through P4 have additional constraints. They are required to originate at the primary vertex, and the transverse momenta of the tracks about this direction is required to balance.

4.3.3 Kinks

A kink is a charged particle that decays into a charged particle and a neutral particle which may go undetected. The kink algorithms are executed after all SSD tracking routines, PWC tracking routines, linking routines and vee routines. The tracks utilized are SSD tracks which do not link and do not point into the M1 aperture. Other requirements for kinks are that PWC tracks from a vee candidate cannot be used, the parent and daughter tracks must have the same charge, and the daughter track must have a smaller momentum than the parent.

For 5-chamber PWC tracks, the z-intersection point is determined by the intersection of the microstrip track and the PWC track in the non-bend view. For 3-chamber PWC tracks, the z-intersection point is determined in the non-bend view, and the track is traced upstream to the parent y-position.

4.3.4 Vertexing

Vertexing in PASS1 is accomplished via an iterative procedure called the "Stand Alone" vertexing algorithm. In this algorithm, all of the SSD tracks are fit to a common vertex. The tracks are then removed one at a time beginning with the one that contributes the most to the χ^2 until the χ^2 falls below some specified value. This forms the first vertex. The procedure is repeated with the remaining tracks until all possible vertices with χ^2 values below the specified cut have been formed. Each time a new vertex is formed, the algorithm attempts to add tracks to it which could have been erroneously discarded or assigned to another vertex. If tracks are not assigned to any vertex they are not permitted to enter any mass combinations.

4.3.5 Momentum Determination

Momentum determination is dependent on the type of track:

- *5-chamber tracks*, identified as those which pass through M2, are traced through its magnetic field. Momentum is determined by means of upstream parameters, downstream parameters, and magnetic field strengths (including fringing effects). Then a least squares fit is performed and reiterated until the track parameters are fairly constant between iterations.

- *3-chamber tracks* (or 4-chamber tracks), have the same momentum determination as described above, except M1 is the bending magnet, the upstream parameters come from the silicon strips, and the downstream parameters come from the PWC's.

- *Unlinked 3-chamber tracks* must first have their vertex determined. The momentum determination through M1 optimizes the best extrapolation of the track to the vertex. If the vertex is unknown, the center of the target is used as a default.

The momentum resolutions are given by:

$$\frac{\sigma_p}{p} = 3.4\% \left(\frac{p}{100\ \text{GeV}}\right) \sqrt{1 + \left(\frac{17\ \text{GeV}}{p}\right)^2}$$

$$\frac{\sigma_p}{p} = 1.4\% \left(\frac{p}{100\ \text{GeV}}\right) \sqrt{1 + \left(\frac{23\ \text{GeV}}{p}\right)^2}$$

for M1 and M2 respectively, where the radical in each expression represents the multiple Coulomb scattering term.

4.3.6 Charged Particle Identification

Čerenkov Identification

The algorithm for the Čerenkov identification begins by observing each cell traversed by a track and all those adjacent to it. If the ADC signals from a track are above a certain pedestal, the track is considered *on*. If the total yield for all cells associated with a given track is less than the predicted yield the track is *off*. The track was labeled *confused* if more than one track could have contributed a significant amount of light to a cell. Based on the particle's momentum and the amount of Čerenkov light emitted, its mass could be identified. Each track was given an ISTATP code based on its identification, which are listed in Table 8.

Muon Reconstruction

The muon reconstruction algorithm starts with extrapolating PWC tracks into the planes of the IM and the OM. Proportional tubes and scintillator counters which

Table 8: ISTATP Codes.

ISTATP Code	Particle
0	Inconsistent Information
1	$e^{\pm}$
2	$\pi^{\pm}$
3	$e^{\pm}$ or $\pi^{\pm}$
4	$K^{\pm}$
6	$\pi^{\pm}$ or $K^{\pm}$
7	$e^{\pm}$, $\pi^{\pm}$ or $K^{\pm}$
8	$p^{\pm}$
12	$K^{\pm}$ or $p^{\pm}$
14	$\pi^{\pm}$, $K^{\pm}$ or $p^{\pm}$
15	$e^{\pm}$, $\pi^{\pm}$, $K^{\pm}$ or $p^{\pm}$

would likely be hit by the hypothesized muon are analyzed for pulse heights, after which a muon decision is made [34].

Electromagnetic Calorimetry

Information supplied by the IE and the OE is instrumental in differentiating electrons from pions and reconstructing neutral showers [30]. Showers are eliminated from PWC tracks using a proximity cut, which requires that no charged tracks are within 5 cm of the centroid of the shower. Isolated showers are analyzed for π^0's, while showers associated with tracks are used to determine the type of track in the calorimeter, if possible. Track hypotheses are formed by determining the location of the actual hits in the strips of the calorimeters, weighing them by their energy, and correcting for the transverse profile of the shower. The transverse and longitudinal energies are passed to two separate discrimination functions which distinguished non-interacting pions and electrons from interacting ones.

4.4 Skims

4.4.1 Light Quark Skim

In order to create manageable data sets in the various analyses, the PASS1 data are skimmed. That is, data are culled from the PASS1 data by imposing certain restrictions. The data set used in this analysis is called the Light Quark Skim and was prepared for the purpose of studying the light quark particles. The following cuts are applied in the Light Quark Skim:

- Events are required to have only one SSD vertex. Events with more than one SSD vertex are most likely charm decays.
- Events are required to have linked track multiplicities of 2 to 6. K_s's and Λ's are counted as single tracks and must point back to the primary vertex.
- Tracks are required to be singly linked to the primary vertex.
- Tracks with momentum greater than 350 GeV are rejected.

Although this skim was not designed to purposely select diffractive events, the resulting sample is rich in them.

4.4.2 Strange Particle Skim

To further reduce the size of the data set, a subskim of the light quark skim was performed at the University of Tennessee. The following cuts are implemented in this skim:

- Charged K's are required to have ISTATP=4 or 12.
- Events are required to have an even number of strange/antistrange tracks.
- Events with an even number of observed charged tracks are required to have a net charge of zero.

- Events with an odd number of observed charged tracks are required to have a net charge of ± 1.

These skim cuts yield a sample of approximately 3 million events from the Light Quark Skim with strange/antistrange tracks.

Chapter 5

Analysis of $f_1(1285)\pi$

5.1 Topologies

The $f_1(1285)\pi$ channel is of particular importance because it is one of the few channels predicted to contain an experimentally accessible hybrid state. In this analysis the $f_1(1285)\pi$ state, denoted here by X, is assumed to decay through the following sequence:

$$X \longrightarrow f_1(1285)\pi^{\pm} \longrightarrow a_0(980)^{\pm}\pi^{\mp} \longrightarrow K_S K^{\pm}$$

The $f_1(1285)$ decays into $a_0(980)^{\pm}\pi^{\mp}$ where the $a_0(980)$ subsequently decays into $K_S K^{\pm}$. This channel only accounts for approximately 10% of the $f_1(1285)$ decays, but due to the nature of the UT strange quark skim, this is the only $f_1(1285)$ decay channel which is available. However, because these events have lower multiplicities, the identification of the tracks has a higher measure of uniqueness than other possible $f_1(1285)\pi$ topologies, which results in a reduction of combinatorial background and a cleaner sample.

The following topologies are studied in this analysis:

$$\gamma N \longrightarrow K_S K^+ \pi^+ \pi^- N'$$
$$\gamma N \longrightarrow K_S K^- \pi^+ \pi^- N'$$
$$\gamma N \longrightarrow K_S K^+ \pi^- \pi^- N'$$
$$\gamma N \longrightarrow K_S K^- \pi^+ \pi^+ N'.$$

K_S represents either K_S or $\overline{K}_S$'s which are indistinguishable, and the recoiling nucleon, N', is not detected. Events where π^0's can be reconstructed are removed from the sample.

Other channels accessible in the UT skim where an $f_1(1285)\pi$ can be formed are the following:

$$\gamma N \longrightarrow K_S K^\pm \pi^\mp \pi^0 N'$$
$$\gamma N \longrightarrow K^+ K^- \pi^\pm \pi^0 N'.$$

The experimental data in both of these reactions reveal evidence for the existence of $f_1(1285)$, but large backgrounds preclude further analysis.

5.2 Mass Spectra

The $K_S K^\pm \pi^\mp$ mass spectrum is shown in Figure 20 where a clear enhancement in the $f_1(1285)$ region is visible. The imposition of the requirement that the $f_1(1285)$ must decay to $a_0(980)^\pm \pi^\mp$ is made by excluding events for which the $K_S K^\pm$ mass exceeds 1010 MeV. Although the Particle Data Group reports that the $a_0(980)$ may be as wide as 300 MeV, this cut was chosen because the average value of the widths listed for $a_0(980)$ is approximately 60 MeV. This cut eliminates some of the $f_1(1285)$ events, but results in a good signal to background ratio in the $a_0(980)^\pm \pi^\mp$ spectrum, while leaving enough events to construct a meaningful $f_1(1285)\pi$ spectrum and decay angular distributions. The $a_0(980)^\pm \pi^\mp$ mass spectrum is shown in Figure 21.

The utility of the $a_0(980)$ mass cut is best illustrated in Figures 22 and 23. Figure 22 is a scatter plot of $K\pi$ masses vs $K\overline{K}\pi$ masses. This plot is dominated

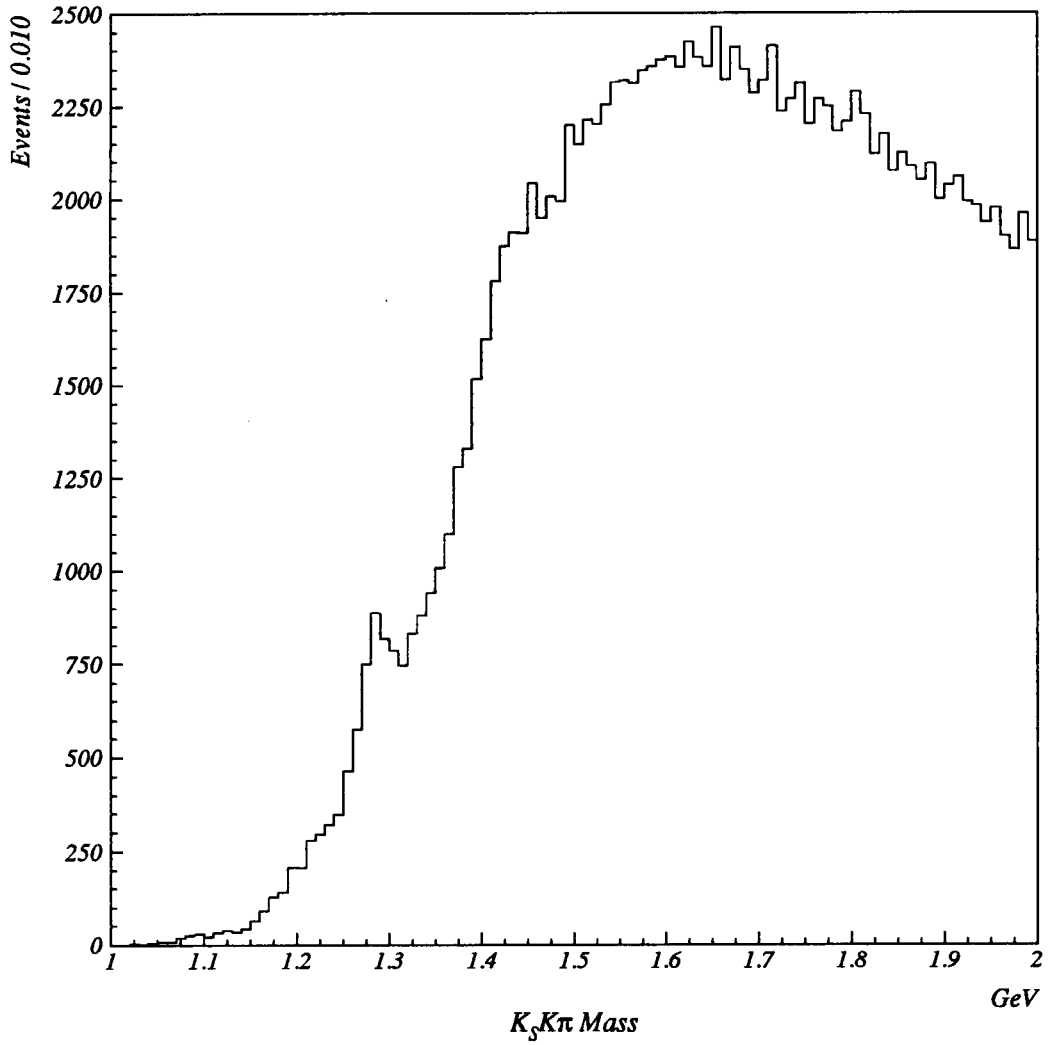

Figure 20: $K_S K^{\pm}\pi^{\mp}$ mass spectrum.

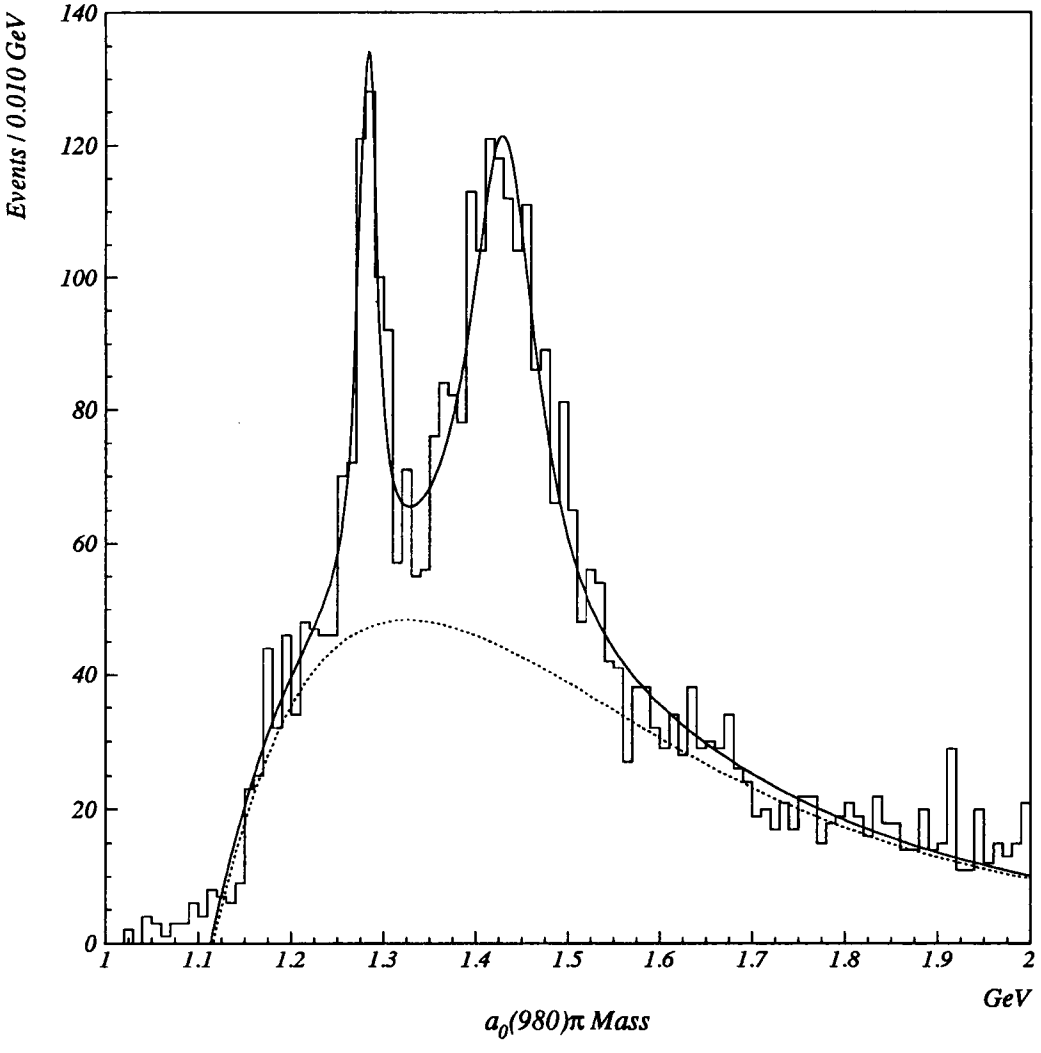

Figure 21: $a_0(980)^{\pm}\pi^{\mp}$ mass spectrum.

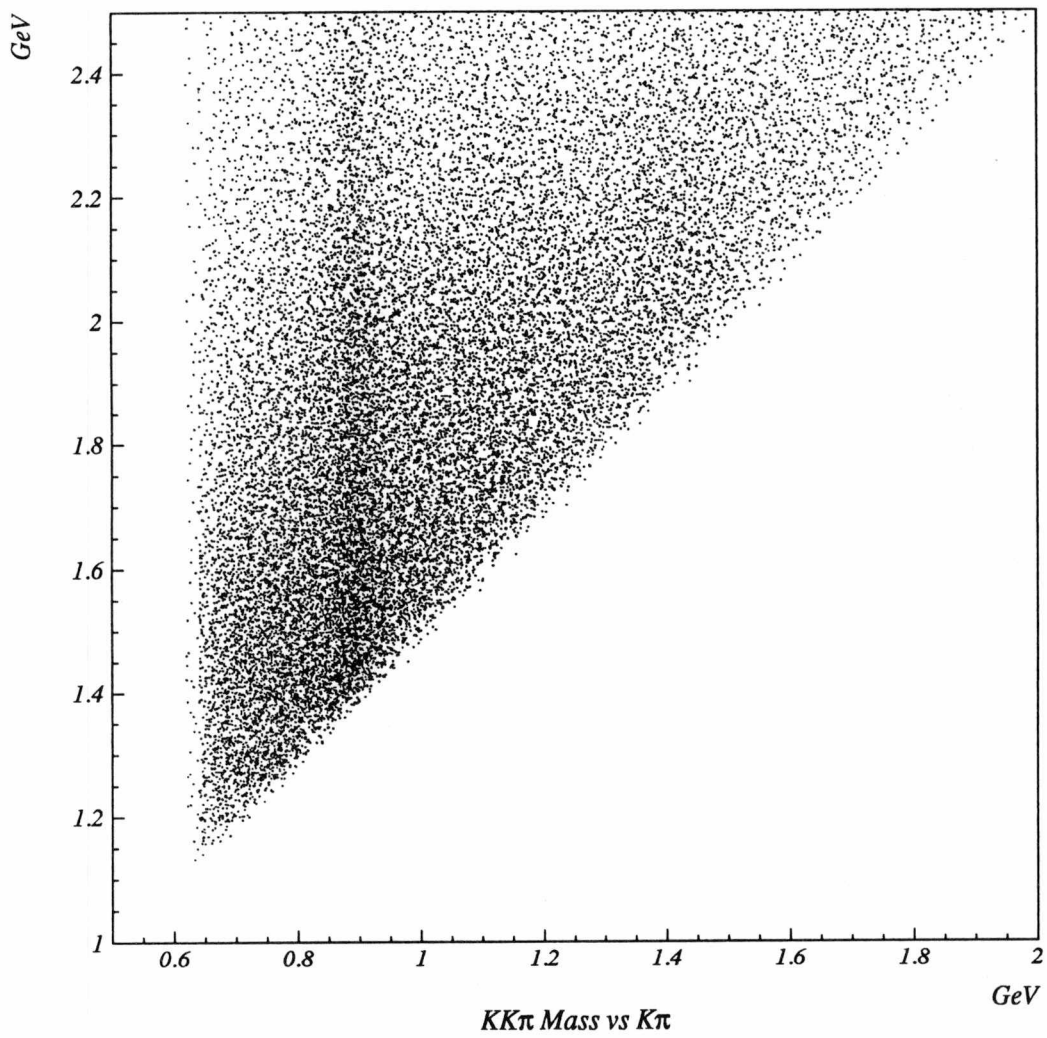

Figure 22: $K_S K^{\pm}\pi^{\mp}$ Mass vs $K\pi$ Mass.

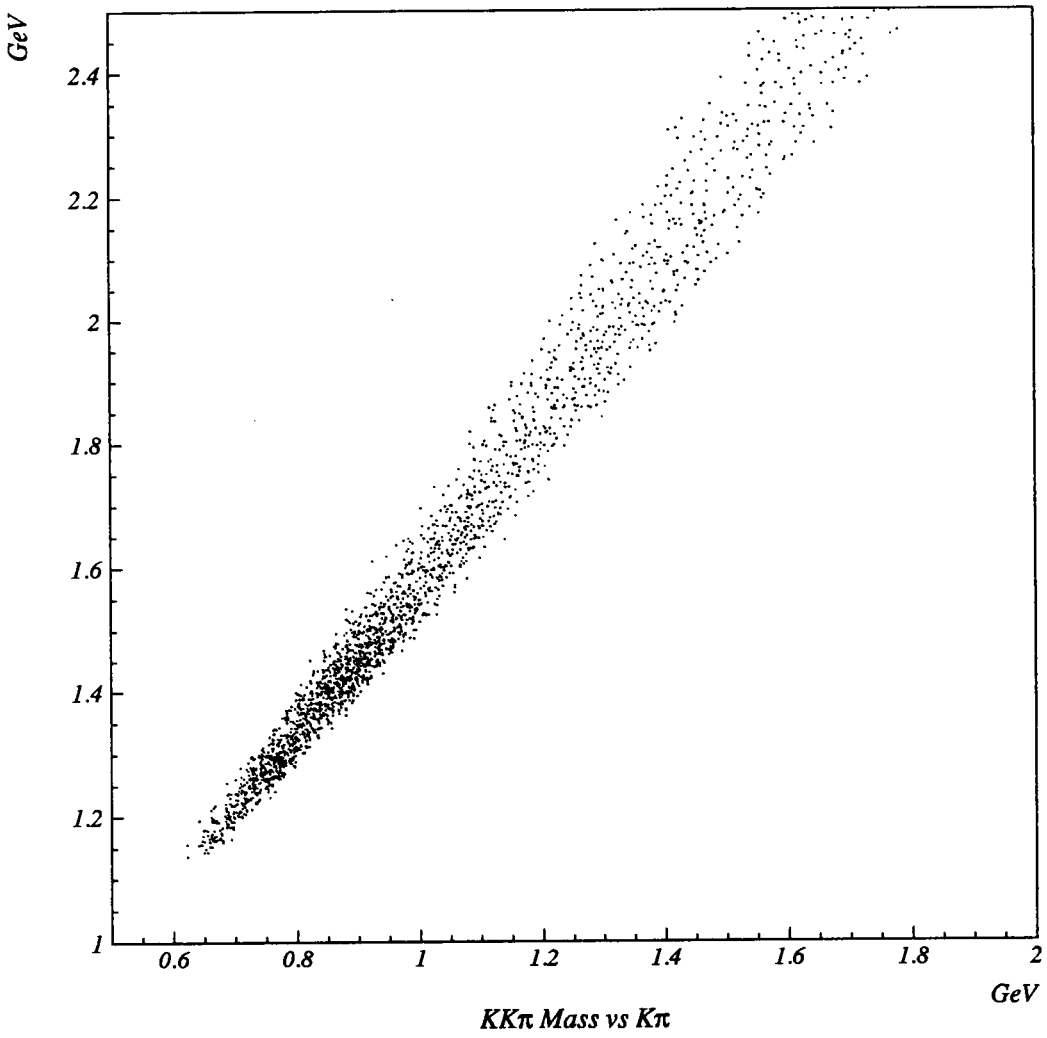

Figure 23: $K_S K^{\pm}\pi^{\mp}$ Mass vs $K\pi$ Mass with $a_0(980)$ cut imposed.

by a dark band of K^* events whose inclusion would severely distort the $f_1(1285)\pi$ data. Figure 23 results when the $a_0(980)$ cut is imposed. It should be noticed that two concentrated areas of events remain at $K\pi$ masses of $\sim$725 MeV and $\sim$900 MeV. The latter area could represent K^* production or a resonance at a $KK\pi$ mass of $\sim$1500 MeV. The enhancements are more clearly delineated in the lego plot in Figure 24.

A fit of the $a_0(980)\pi$ mass spectrum was carried out in the following manner. First a background was constructed by plotting the invariant mass formed with an $a_0(980)$ from one event and a π from another. This background was fit to the following shape:

$$background = (A + Bx + Cx^2)(1 - De^{E-Fx})$$

A fit to the background is found in Figure 25, and the fitted background parameters can be found in Table 9. This background shape is used, in conjunction with two simple Breit-Wigner distributions, to construct the fit to the $a_0(980)\pi$ mass spectrum in Figure 21. The parameters for the resulting Breit-Wigner distributions are listed in Table 10.

The narrow peak is fit to a mass of 1282 ± 2 MeV with a width of 23.2 ± 0.7 MeV, both of which are quite consistent with the Particle Data Group's mass and width for the $f_1(1285)$ of 1282 ± 5 MeV and 24 ± 3 MeV respectively.

The wide peak is fit by a simple Breit-Wigner of mass 1430 ± 3 MeV and width of 87.8 ± 5.9 MeV. There are two known states in this mass region listed by the Particle Data Group. The first one is the $f_1(1420)$ resonance which is reported to have a mass of 1426.8 ± 2.3 MeV and a width of 52 ± 4 MeV. The second is the $\eta(1440)$ with a reported mass of 1420 ± 20 MeV and width of 60 ± 30 MeV. Both resonances are reported to decay dominantly to $K\overline{K}\pi$, with the states $a_0(980)\pi$ and K^*K listed as intermediate decay modes.

Since the E687 data reproduce the accepted mass and width of the $f_1(1285)$ almost exactly, it is likely that the more massive enhancement is either the $\eta(1440)$ or a combination of it and the $f_1(1420)$. There could also be a contribution from

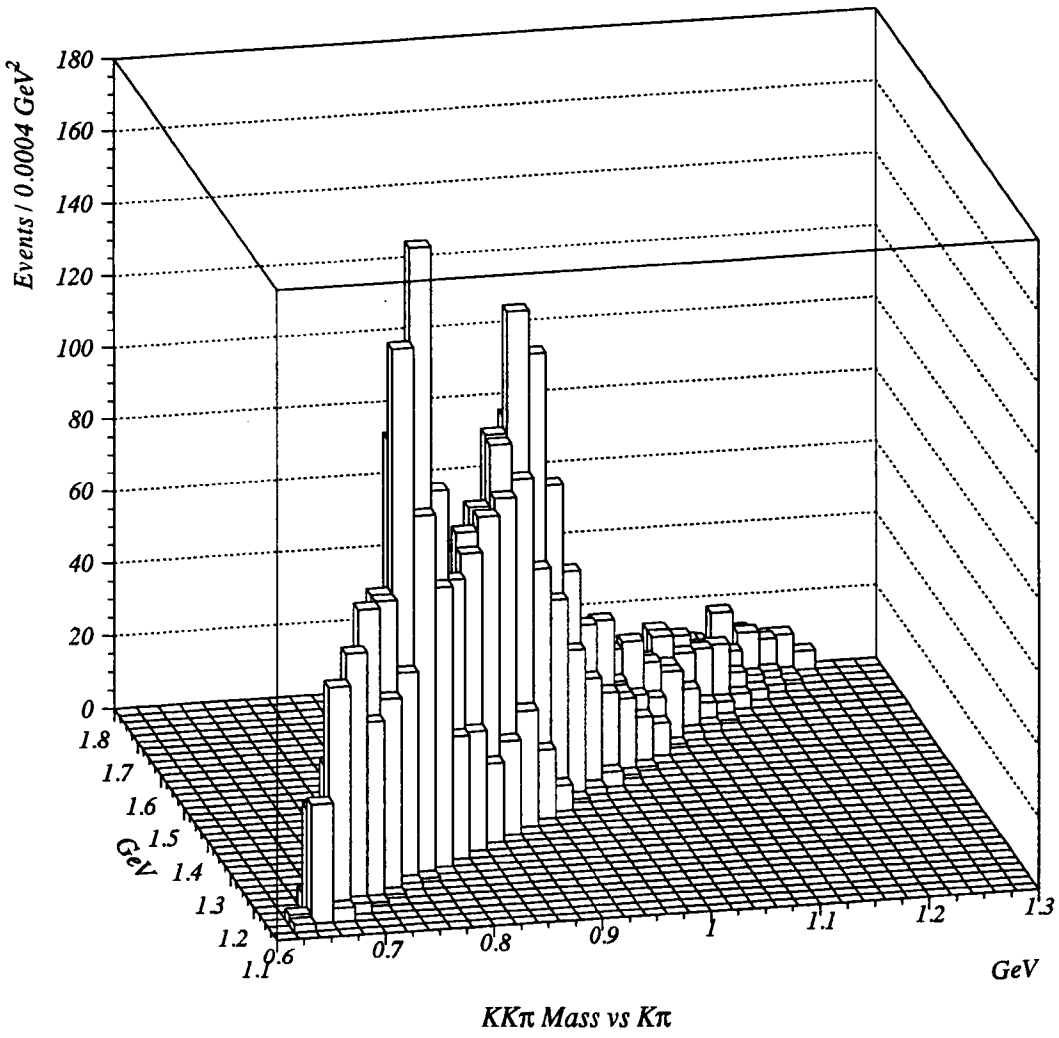

Figure 24: Lego plot of $K_S K^{\pm}\pi^{\mp}$ mass vs $K\pi$ mass with $a_0(980)$ cut imposed.

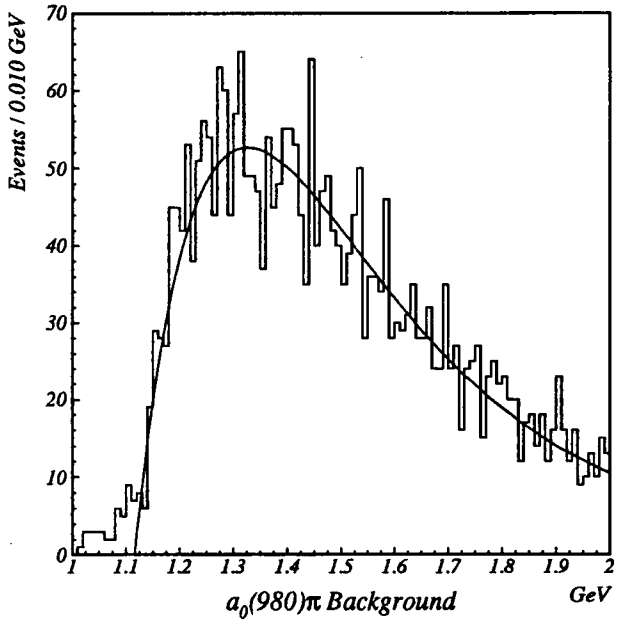

Figure 25: Background constructed for $a_0(980)^{\pm}\pi^{\mp}$ mass spectrum.

Table 9: Background fitting parameters for the $a_0(980)^{\pm}\pi^{\mp}$ mass spectrum.

Parameter	Value
A	−9.450
B	11.37
C	−2.601
D	−4.925
E	8.040
F	4.331
scale factor	0.9188

Table 10: Resonance fitting parameters for $a_0(980)^{\pm}\pi^{\mp}$ mass spectrum.

Mass (MeV)	Width(MeV)	Significance(σ)	Number of Events
1282 ± 2	23 ± 1	10.79	309 ± 29
1430 ± 3	88 ± 6	20.52	1063 ± 52

direct K^* production (Figures 23 and 24). As no further analysis of this enhancement is pursued in this dissertation, no effort to further quantify this state is made. These observations are quite similar to those of Lee *et. al* [21], at BNL, who studied the reaction $\pi^- p \longrightarrow \overline{K}_S K^+ \pi^- \pi^- p$. In this experiment, the $\overline{K}_S$ and K^+ are assumed to be the decay products of an $a_0(980)^+$, while the $a_0(980)^+$ and a π^- are the results of $f_1(1285)$ decay. In particular, they observe a narrow $f_1(1285)$ along with a higher mass enhancement in the $a_0(980)\pi$ mass spectrum. This latter enhancement has been fit at the University of Tennessee (UT) and found to correspond to a mass of 1434 ± 4 MeV with a width of 92 ± 8 MeV. These values are virtually identical to the UT observation in the E687 data.

In Chapter 2 it was observed that if VMD and OPE are assumed for the E687 data, and if the exchange mechanism is ρ exchange for the BNL data, then the meson interaction vertices in the two experiments are identical ($\pi\rho, X \rightarrow f_1(1285)\pi$). (See Figure 26.) Because the $f_1(1285)\pi$ is a charged system, the production of this state from photon interactions requires an isovector exchange mechanism, which again suggests OPE. Because the photon predominantly manifests itself as a ρ meson in VMD, OPE is likely if G-parity is to be conserved. Pion exchange has been previously observed in photoproduction by G. T. Condo *et. al.* [41] in SLAC hybrid bubble chamber data and by G. R. Blackett [30] in an analysis of 3π photoproduction in E687.

The $f_1(1285)\pi$ mass spectrum is shown in Figure 27 with the requirement, 1260 MeV $< Mass(a_0(980)\pi) <$ 1310 MeV, for the $f_1(1285)$. The fitting parameters from this mass spectra are listed in Table 11. A background is constructed by

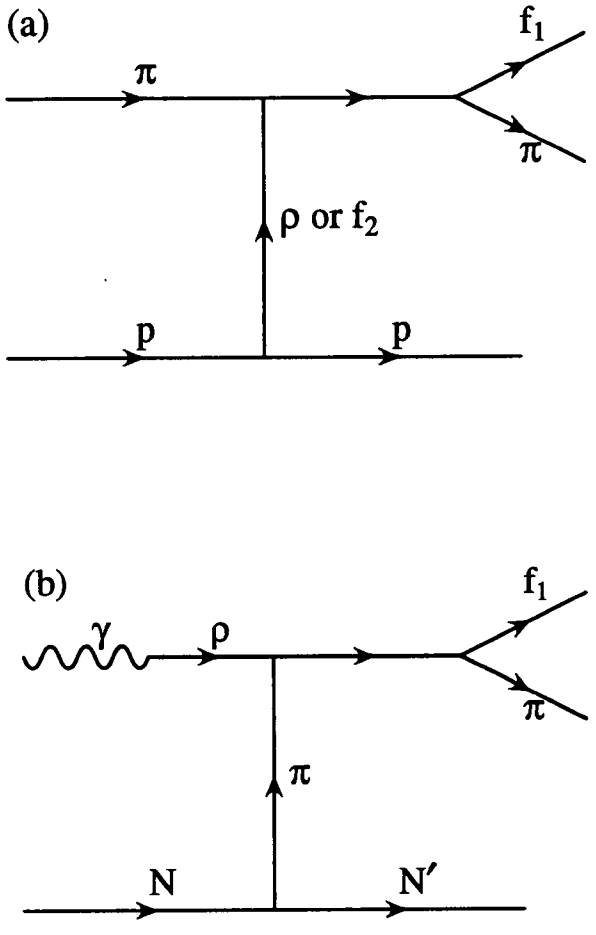

Figure 26: Diagrams of $f_1(1285)\pi$ production at (a) BNL and (b) E687 at FNAL.

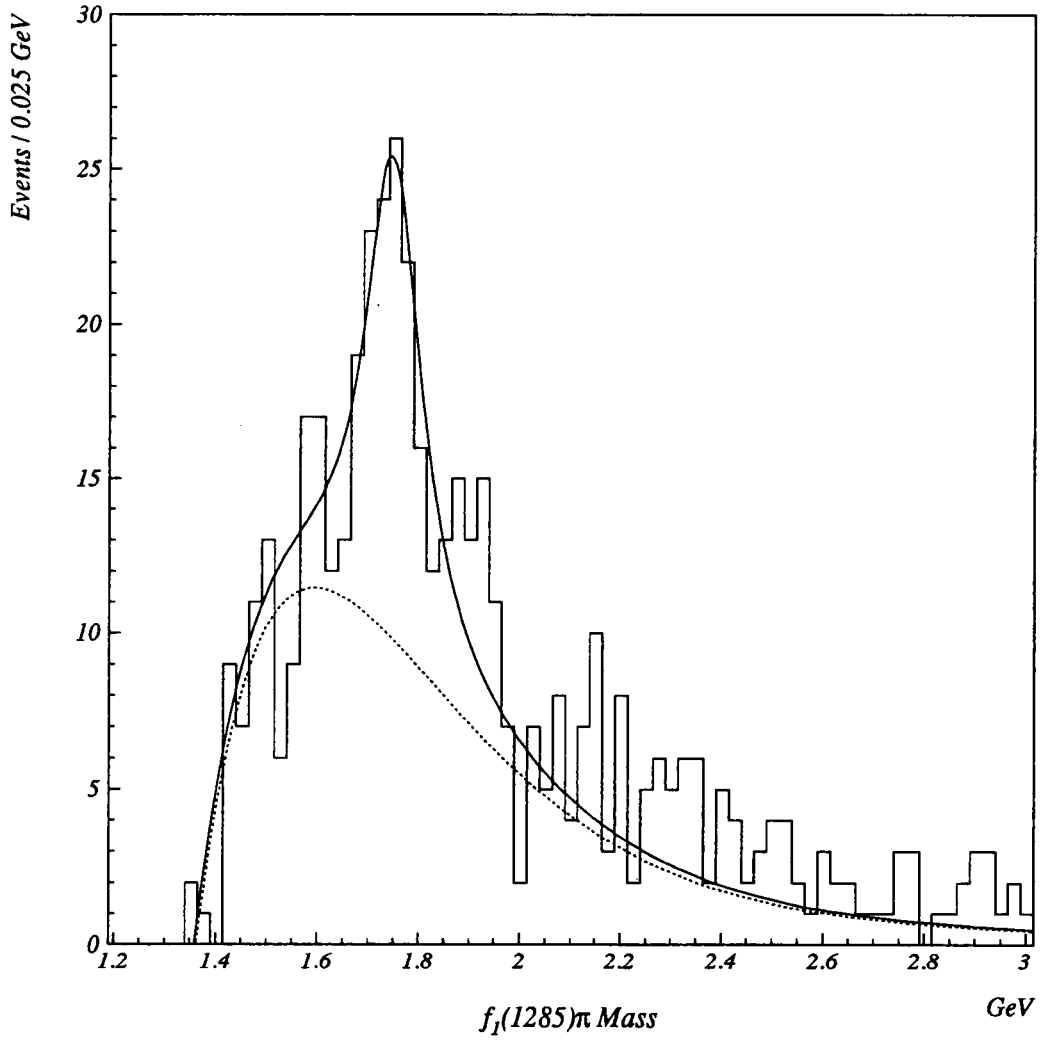

Figure 27: $f_1(1285)\pi$ mass spectrum.

Table 11: Resonance fitting parameters for the $f_1(1285)\pi$ mass spectrum.

Parameter	Value
Mass	1748 ± 12 MeV
Width	136 ± 30 MeV
Number of Events	134 ± 18
Significance	7.3σ

creating an $f_1(1285)\pi$ invariant mass using an $f_1(1285)$ from one event with a π from another, similar to the determination of the $a_0(980)\pi$ background. The background is shown in Figure 28, and the background fitting parameters are listed in Table 12. The $f_1(1285)\pi$ mass was fit using a scaled version of the background fit and a single Breit-Wigner distribution. The mass and width of the resulting Breit-Wigner distribution are 1748 ± 12 MeV and 136 ± 30 MeV respectively. The data generally lie above the background for masses in excess of 2000 MeV which could indicate the production of another (broad) resonance at mass of about 2300 MeV. However, the data are insufficient to substantiate such a claim.

5.3 Angular Analysis

One of the tools available to determine the spin and parity assignments, J^P, for an unstable particle is the analysis of its decay angular distributions. Here the decay of the $f_1(1285)\pi$ resonance, previously referred to as X, with unknown J^P, decays into a π of spin 0 and an $f_1(1285)$ of spin 1, which subsequently decays into two spin 0 particles, $a_0(980)$ and π, followed by the $a_0(980)$ decay into two more spin 0 particles, $K^{\pm}$ and K_S.

The analysis is particularly simple in the helicity frame of the $f_1(1285)$. This is the rest frame of the $f_1(1285)$ with the z-axis taken to be the direction of the $f_1(1285)$ in the rest frame of X. A pictorial definition of this reference frame is

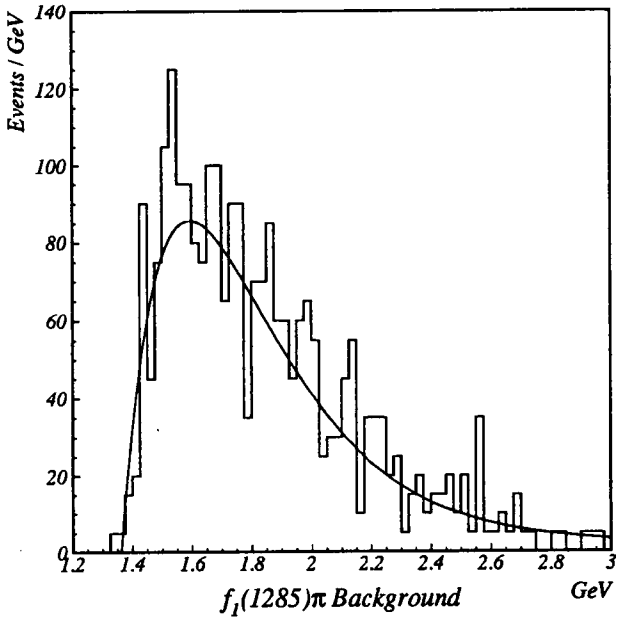

Figure 28: $f_1(1285)\pi$ background.

Table 12: Background fitting parameters for $f_1(1285)\pi$ spectrum.

Parameter	Value
A	−9.736
B	9.710
C	−1.881
D	−14.58
E	8.022
F	3.905
scale factor	0.1338

given in Figure 29. The expected angular distributions of the helicity angle, θ_H, are listed in Table 13 for all possible J^{PC} assignments for X with $J < 3$ [42]. States with negative charge conjugation will not occur if G-parity is conserved in the decay of the X particle. A serendipitous feature of this angular distribution is that it is independent of the polarization of the parent particle, X. Thus, although it has been argued that OPE is the most likely production mechanism for the charge exchange photoproduction of X, the decay angular distribution of the $f_1(1285)$, in its helicity frame, is independent of this assumption.

The acceptance corrected θ_H polar distribution for the X region (1650 MeV $\leq Mass(X) \leq$ 1820 MeV) is shown in Figure 30. Of the distributions listed in Table 13, the best fit occurs for the $J^{PC} = 1^{-+}$ hypothesis [1]. While other angular distributions are often used to determine J^{PC} values they will not be used here. The s-channel helicity frame is inappropriate because of the patently charge exchange nature of the production mechanism. If OPE is the production mechanism, the relevant coordinate system is the Gottfried-Jackson frame which utilizes the incoming beam direction in the rest frame of X as the z-axis. Since this is not always a well-determined quantity in this experiment, the angular distributions will contain unknown biases.

The observation of a $J^{PC} = 1^{-+}$ partial wave suggests the existence of an exotic state. The BNL group reported a resonance at 1700 MeV with $J^{PC} = 1^{++}$ together with a $J^{PC} = 1^{-+}$ wave extending from 1600 MeV to 2200 MeV. The E687 data, while indicating the production of a relatively narrow resonance at ~1750 MeV with $J^{PC} = 1^{-+}$, contain no evidence for the production of a $J^{PC} = 1^{++}$ state. The E687 data also contain, at most, marginal evidence for the production of any resonance at masses in excess of 2000 MeV.

It is possible to fit the $f_1(1285)\pi$ mass spectrum to a two resonance parameterization with the additional resonance occurring at ~1900 MeV. This fit has

[1] Although the $J^{PC} = 2^{++}$ possibility cannot be totally excluded, when the distribution was fit to a function of the form $A + B\cos^2\theta$, the value of the $\cos^2\theta$ coefficient B was less that 2% of the constant term A. This is clearly suggestive of a flat distribution.

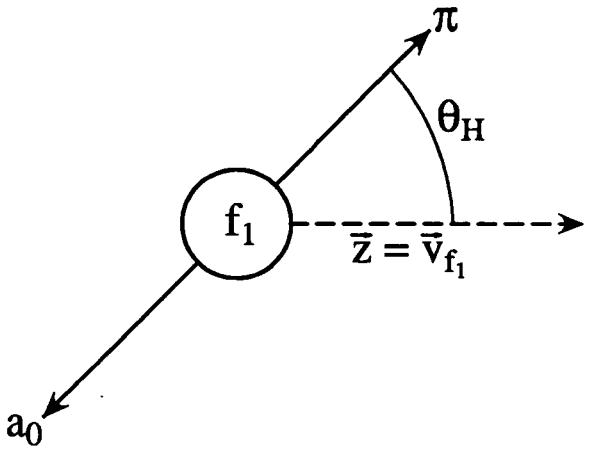

Figure 29: Schematic of the helicity reference frame.

Table 13: Helicity angular distributions for various J^{PC} of resonance X.

J^{PC}	Angular Distribution
0^{++}	$\cos^2\theta_H$
1^{++}	$\sin^2\theta_H$
1^{-+}	*constant*
2^{++}	$3+\cos^2\theta_H$
2^{-+}	$\sin^2\theta_H$

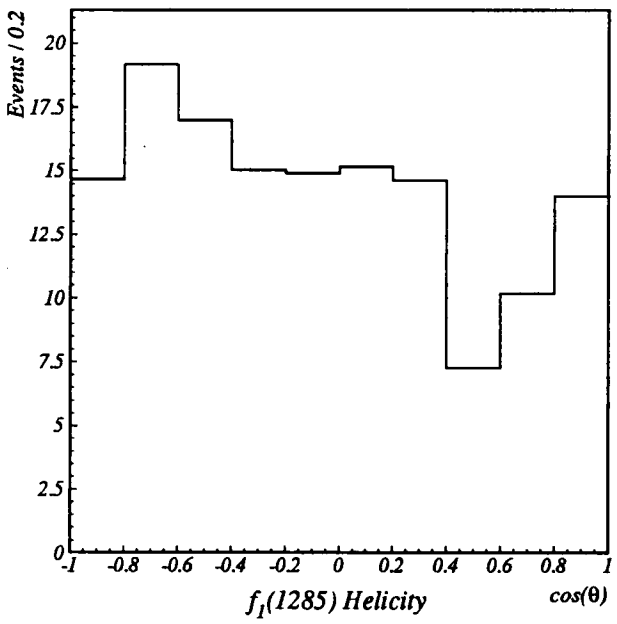

Figure 30: Angular distribution in the helicity reference frame for the $f_1(1285)\pi$ resonance.

approximately the same χ^2 as the single resonance fit. However, since the decay angular distribution of the additional events is consistent with that of the 1750 MeV mass region, there is no compelling reason for preferring the presence of a second resonance in the data.

The hybrid candidate $X(1775)$ ($I^G J^{PC} = 1^-?^{-+}$) [25], observed in lower energy photoproduction, is listed by the Particle Data Group with a mass of 1776 ± 13 MeV and a width of 155 ± 40 MeV. Both of these values approximate those observed for the X in the E687 data. This is of interest because $\rho\pi$ is one of the decay modes of $X(1775)$ - hence the existence of a $\pi\rho X(1775)$ vertex which is quite similar to the $\pi\rho(f_1(1285)\pi)$ vertex in E687. Although the $\rho\pi$ channel is expected to be suppressed in most flux tube predictions, Close and Page [24] suggest that its contribution is not negligible. They predict the $\rho\pi$ partial widths of the suggested $J^{PC} = 1^{-+}$ state to be approximately $5 - 20$ MeV.

In conclusion, there is an enhancement, in the E687 data, in the $f_1(1285)\pi$ mass spectrum at a mass of 1748 ± 12 MeV with a width of 136 ± 30. The $f_1(1285)$ helicity angular distribution favors $J^{PC} = 1^{-+}$. This observation is consistent with an earlier photoproduction experiment where evidence was presented for a (primarily) $\rho\pi$ state with a mass of 1776 ± 13 and a width of 155 ± 40 whose decay angular distributions favored the assignment $J^{PC} = 1^{-+}$.

Chapter 6

Analysis of $\phi\eta$

At the present time, the physics literature contains very little information regarding the $\phi\eta$ channel. The Particle Data Group reports a J/ψ decay to $\phi\eta$ with a very small partial width, but does not report $\phi\eta$ to be a decay mode for any light quark meson resonance. It has been briefly discussed by B. Delcourt *et. al.* [43] in an analysis of $p\bar{p}$ interactions, but their data were insufficient to claim the observation of a resonance.

In E687 $\phi\eta$ is quite an accessible channel. Events were chosen from the topology $\gamma N \longrightarrow K^+K^-\pi^+\pi^-\pi^0 N'$. Both the ϕ and the η are very narrow states, and both occur close to threshold, in the decay channel investigated, which minimizes the background under the resonances. If the $\phi\eta$ resonance is denoted by Y, its sequential decay can be expressed as:

$$Y \longrightarrow \phi\eta \begin{cases} \longrightarrow \pi^+\pi^-\pi^0 \\ \longrightarrow K^+K^- \end{cases}$$

A diagram of this reaction is shown in Figure 31. The mechanism involved is assumed to be Pomeron exchange.

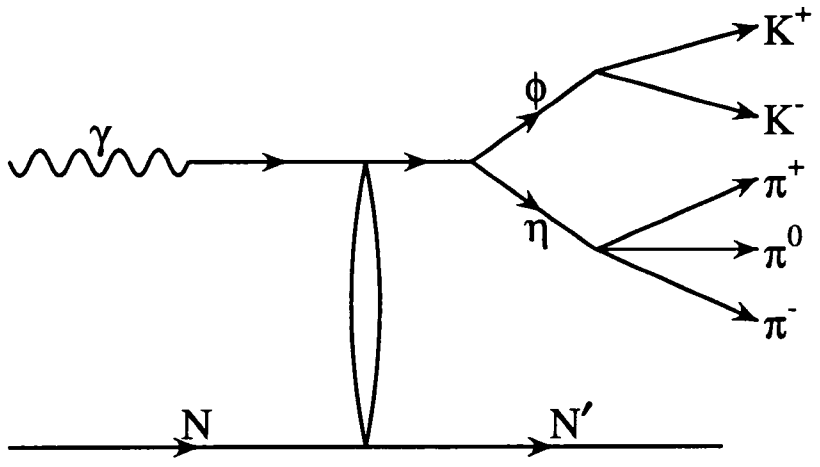

Figure 31: Feynman diagram for the diffractive photoproduction of a $\phi\eta$ state.

6.1 $\phi\eta$ Mass Spectra

The K^+K^- mass spectrum is shown in Figure 32(a). If an η cut is imposed such that 530 MeV $< Mass\,(\pi^+\pi^-\pi^0) <$ 570 MeV, the ϕ peak remains and is actually enhanced relative to the background as shown in Figure 32(b). The $\pi^+\pi^-\pi^0$ mass spectrum, shown in Figure 32(c), displays prominent η and ω resonances. When a ϕ cut is imposed on the K^+K^- mass such that 1010 MeV $< Mass\,(K^+K^-) <$ 1030 MeV, the mass spectrum in Figure 32(d) results. Both the η and ω resonances remain significant features of the spectrum with with very little background in the η region. These spectra illustrate strongly associated $\phi\eta$ photoproduction. This association is also quite evident in the scatter plot shown in Figure 33 and the lego plot shown in Figure 34. The mass spectra in Figures 32, 33 and 34 are restricted to events with only two experimentally detected photons in the IE which reconstruct to form the π^0.

The $\phi\eta$ mass spectrum is shown in Figure 35. This spectrum is dominated by an enhancement corresponding to a mass of 1914 $\pm$ 33 MeV and a width of

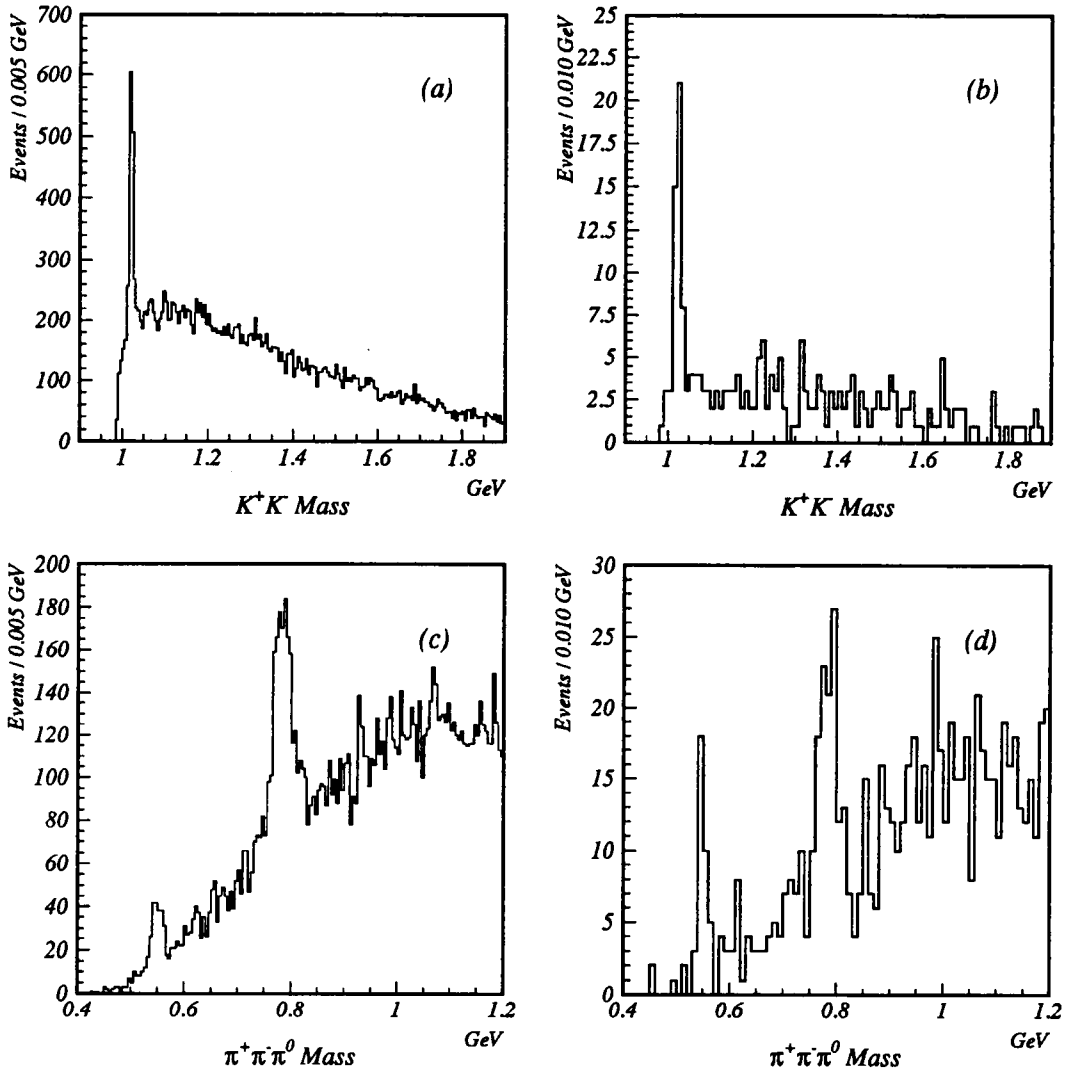

Figure 32: Mass spectra of (a) the K^+K^- mass, (b) the K^+K^- mass with an η mass cut, (b) the $\pi^+\pi^-\pi^0$ mass and (d) the $\pi^+\pi^-\pi^0$ mass with a ϕ cut.

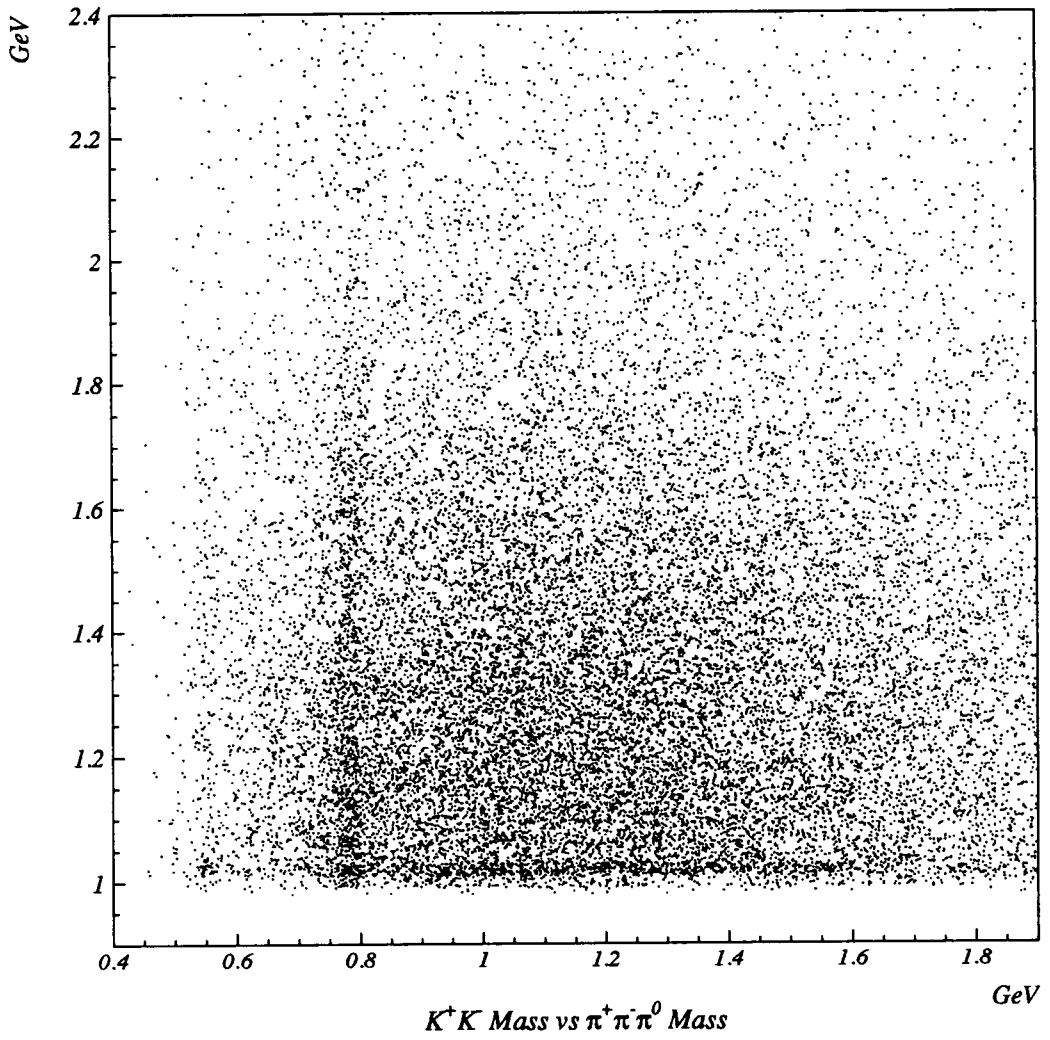

Figure 33: Scatter plot of the K^+K^- Mass vs the $\pi^+\pi^-\pi^0$ Mass.

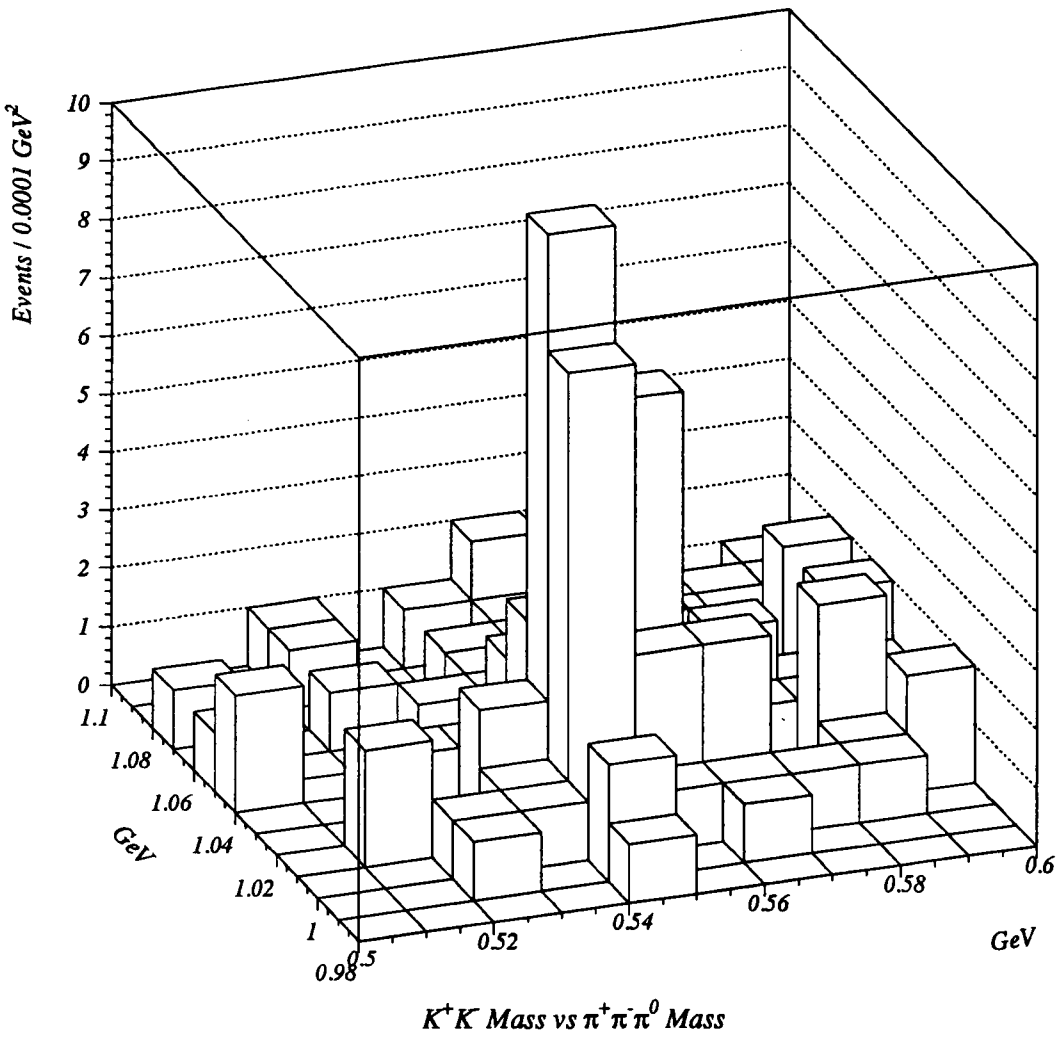

Figure 34: Lego plot of the K^+K^- Mass vs the $\pi^+\pi^-\pi^0$ Mass.

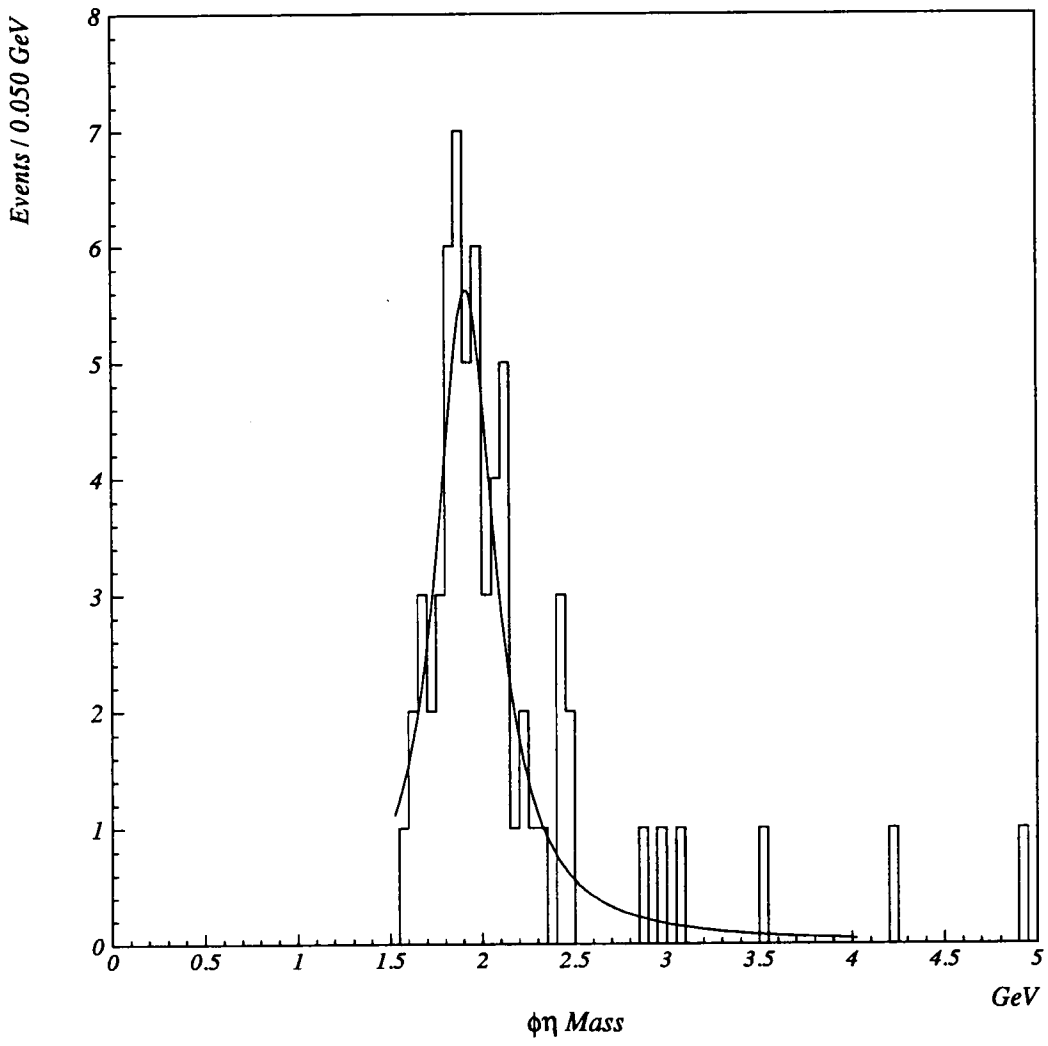

Figure 35: $\phi\eta$ mass spectrum.

389 ± 115 MeV. The absence of any $\phi\eta$ signal in the J/ψ mass region is consistent with its known cross sections and branching ratios.

Close and Page [24] predict the existence of two possible hybrid resonances in this mass region which have partial decay widths to the $\phi\eta$ final state. These states have $J^{PC} = 1^{--}$ and $J^{PC} = 1^{+-}$, and total widths of 230 MeV and 545 MeV respectively. The $J^{PC} = 1^{--}$ state is also predicted to decay to $\phi\eta'$, K^*K, $K_2^*(1430)K$, $K_1(1270)K$ and $K_1(1400)K$, while the $J^{PC} = 1^{+-}$ state is also expected to decay to $\phi\eta'$, K^*K, $K_2^*(1430)K$, $K_1(1270)K$ and $K_0^*(1430)K$. These channels are essentially unavailable for analysis in this experiment because of large backgrounds due to competing processes. It is also possible that a $\phi\eta$ state could represent the second radial excitation of the $\phi(1020)$. Since vector meson production dominates photon interactions, the production of one of these vector mesons may be enhanced in this experiment. Although this analysis is limited by low statistics, the very small background suggests that the decay angular distributions may be employed to determine the J^{PC} quantum numbers of the resonance.

6.2 Angular Analysis

The decay angular distributions of the presumed $\phi\eta$ state are studied in the three reference frames illustrated in Figure 36. The first two, which are the helicity frame of the main resonance and the canonical frame of the ϕ, are appropriate systems for diffractively produced resonances (Pomeron exchange). The third frame is the helicity frame of the ϕ. This frame is advantageous since the angular distribution is independent of the helicity of the decaying particle, and therefore independent of the exchange mechanism involved in its production. The events used in the analysis were required to have a $\phi\eta$ mass between 1750 and 2150 MeV. The expected angular distributions for the $J^{PC} = 1^{--}$ state and the $J^{PC} = 1^{+-}$ state are listed in Table 14 [42]. The helicity angular distribution of the main resonance and the canonical distribution of the ϕ are calculated under the assumption that Pomeron

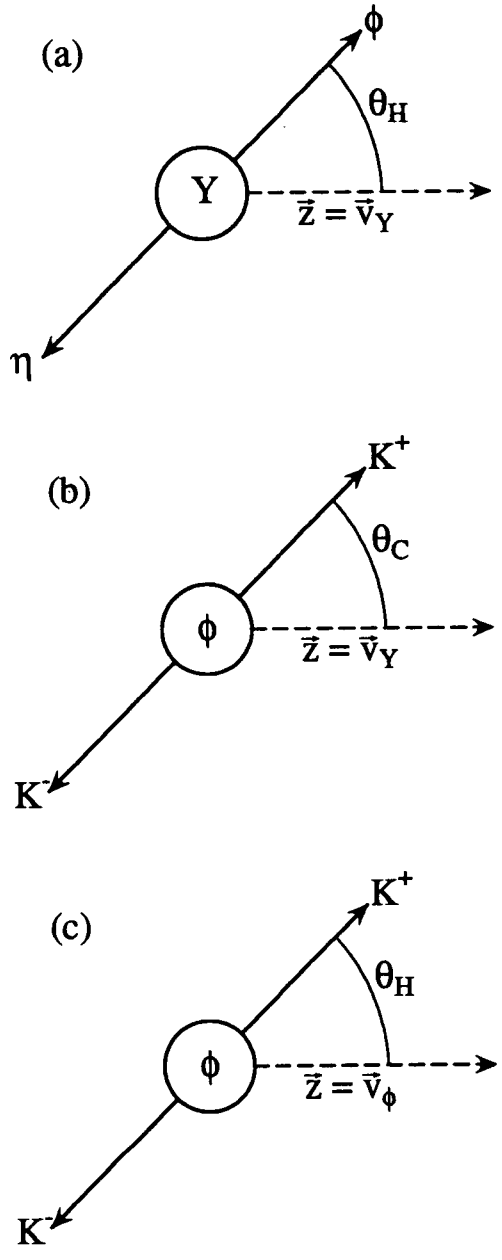

Figure 36: Schematic diagrams of (a) the helicity angle in the rest frame of the resonance (b) the canonical angle in the rest frame of the ϕ, and (c) the helicity angle in the rest frame of the ϕ.

Table 14: Angular distributions for the $\phi\eta$ resonance.

J^{PC}		Helicity(Y)	Canonical(ϕ)	Helicity(ϕ)
0^{--}		*constant*	$1+\sin^2\theta_C$	$\cos^2\theta_H$
1^{--}		$1+\cos^2\theta_H$	$1+\cos^2\theta_C$	$\sin^2\theta_H$
1^{+-}	S wave	*constant*	$\sin^2\theta_C$	*constant*
	D wave	$5-3\cos^2\theta_H$	$6+\sin^2\theta_C$	$1+3\cos^2\theta_H$
2^{--}		$1+\cos^2\theta_H$	$1+\cos^2\theta_C$	$3+\cos^2\theta_H$

exchange is the production mechanism. The acceptance corrected angular distributions are shown in Figure 37. The helicity distribution of the main resonance and the canonical distribution of the ϕ both appear to have a $1+\cos^2\theta$ component, which is consistent with the $J^{PC}=1^{--}$ hypothesis and inconsistent with both the S and D wave $J^{PC}=1^{+-}$ hypotheses. The helicity angular distribution of the ϕ clearly has a $\sin^2\theta$ component, which is again consistent with expectations for the $J^{PC}=1^{--}$ state and inconsistent for both the S and D waves of the $J^{PC}=1^{+-}$ state. The angular distributions are also not consistent with $J^{PC}=0^{--}$ or 2^{--}.

The $\phi\eta$ mass spectrum and the decay angular distributions are indicative of the photoproduction of a vector meson with a mass of 1914 MeV, with a width of approximately 389 MeV. Because of the ordinary vector meson quantum numbers of this state, one cannot unambiguously classify it as a hybrid. This is especially so since the second radial excitation of the ϕ is expected in this mass region [44]. However, because of the strong correlation between theoretical predictions and experimental data, there is a distinct possibility that a hybrid state has been observed in this analysis.

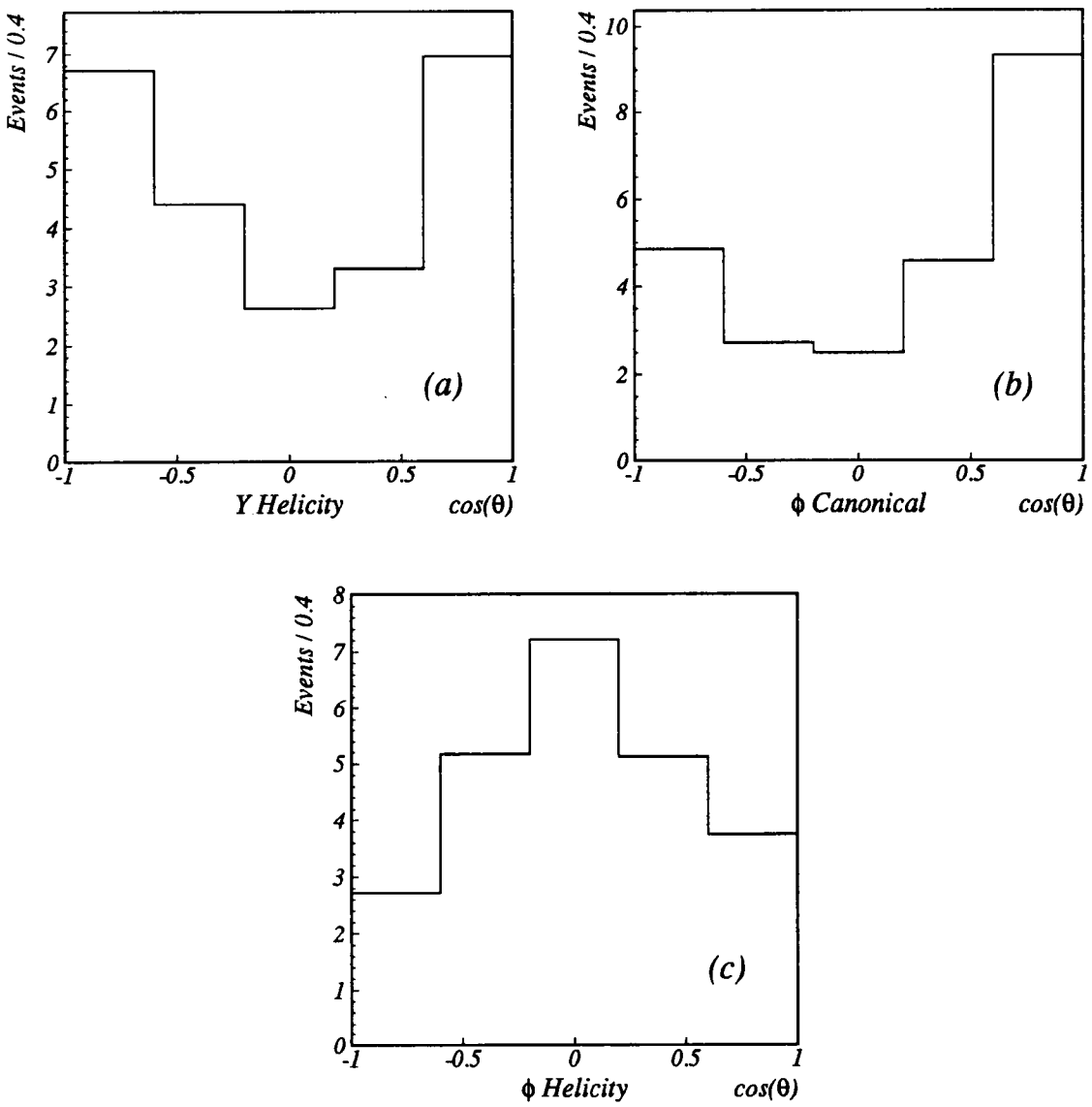

Figure 37: Acceptance corrected angular distributions for (a) the helicity frame of the $\phi\eta$ resonance, (b) the canonical frame of the ϕ and (c) the helicity frame of the ϕ.

Chapter 7

Monte Carlo Analysis

SROGUE is a Monte Carlo program developed by the E687 collaboration to study efficiencies in the E687 data. SROGUE consists mainly of two packages of code. The first, called GENERIC, generates an event, and the second, ROGUE, simulates the decay particles traversing the E687 spectrometer. The output is called a "faketape" and is identical in structure to the actual raw data tapes. This allows the output to be processed with the same reconstruction and analysis routines as the real data.

7.1 Description of SROGUE

7.1.1 GENERIC

The physics problem is defined for the GENERIC code in an interaction specification file called a CHAT file. In the CHAT file the user can adjust parameters and define a specific decay chain. Only one decay mode at a time can be specified in a CHAT file.

Initially, GENERIC generates an electron beam which interacts in the lead radiator. The tagged electron energy is adjusted to a spread around 350 GeV, based on observations in the real data. Both the RESH and the BGM/BCAL are

set to operate in a pile-up mode. This allows for multiple electrons per event, as in the real data. The probability of the photon generating an event inside the target is determined by means of a step function over the target length. Multiple bremsstrahlung is permitted but only a single photon is allowed to interact with the target. Other photons produced in multiple bremsstrahlung processes are allowed to produce so-called "embedded pairs" (e^+e^- pairs) in the target. This has been determined to be about a 17% effect [44]. Any remaining non-interacting photons are traced through to the BGM/BCAL.

Strong decays of resonances and production mechanisms are also performed in GENERIC. One pion exchange and Pomeron exchange (beam diffraction) are chosen as the production mechanisms for the $f_1(1285)\pi$ and $\phi\eta$ events respectively. Although the inclusion of jets is an option, they are not employed in this analysis.

The phase space distributions are calculated with another Monte Carlo package called SAGE. All resonances are assumed to be Breit-Wigner distributions with uniform phase space.

7.1.2 ROGUE

After the interaction is created in GENERIC, the ROGUE routines trace the particles through the detector until they decay into stable particles (this analysis allowed for in-flight decays), fail to pass through an aperture, or otherwise exit the spectrometer. Natural stopping points (such as places where a particle may deposit energy in a detector, places where a particle may multiple Coulomb scatter, and so on) are analyzed to check the particle status and the probability for any physical processes to occur. For each device in the spectrometer traversed by a particle, ROGUE generates an appropriate response including noise and shared hits.

The user has the option of not imposing any triggers for geometric efficiencies, imposing just the Master Gate triggering, or imposing both the Master Gate and Second Level triggering. Since several Master Gate and Second Level triggers were used during the 90-91 run, events with these triggers are generated proportionately

to those in the real data.

7.2 Application to Data

Since there were four topologies in the $f_1(1285)\pi$ channel, separate code was required for each of them. The $\phi\eta$ code on the other hand had a single unique topology. The efficiencies in this analysis are determined by dividing the value of each bin in the reconstructed spectra by the value of each bin in the generated spectra.

7.2.1 Mass Efficiencies

The mass efficiencies for the $K_S K\pi\pi$ channel and the $K^+K^-\pi^+\pi^-\pi^0$ channel are shown in Figure 38. Both appear relatively constant in the mass regions where possible hybrid states are expected in the data. The lower efficiency in the $K^+K^-\pi^+\pi^-\pi^0$ channel results from requiring that the π^0's are reconstructed from photons in the IE only. It is likely that this requirement also accounts for the increasing efficiency at higher mass in this channel. Because the π^0's in the higher mass states are more likely to be produced in the forward direction, the probability of their detection should be enhanced.

7.2.2 Beam Characteristics

The parameters used to calculate the incident photon energy were generated and reconstructed with the SROGUE package. These parameters, along with the calculated incident photon energy are plotted in Figure 39 for the $K_S K\pi\pi$ channel. Likewise the spectra of these parameters in the real data are presented in Figure 40. For both the real and the Monte Carlo data, if the incident photon energy is less than the energy of the outgoing tracks, the incident photon energy is taken to be the energy of the outgoing tracks. The corresponding plots in the $K^+K^-\pi^-\pi^+\pi^0$

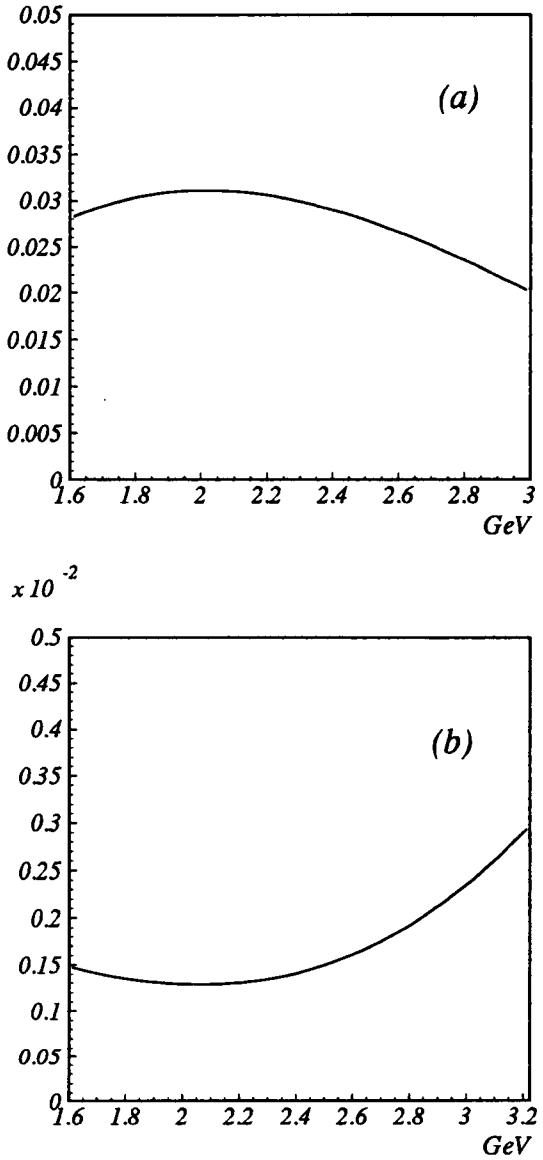

Figure 38: Mass efficiencies for the $K_S K\pi\pi$ channel and the $K^+K^-\pi^+\pi^-\pi^0$ channel.

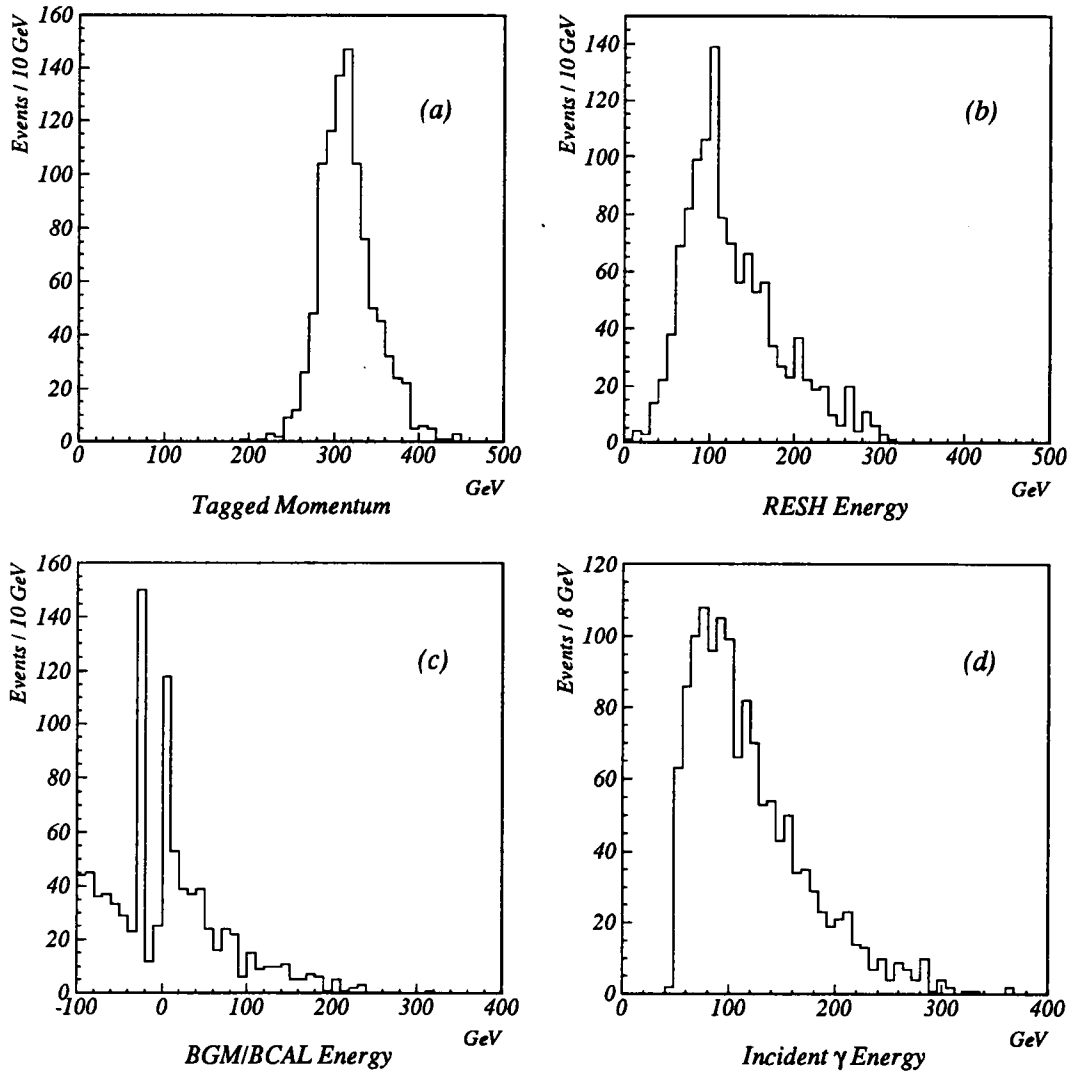

Figure 39: Beam characteristic plots of Monte Carlo data for the $K_S K\pi\pi$ channel: (a) The momentum of the tagged electron. (b) Energy recorded in the RESH. (c) Energy recorded in the BGM/BCAL. (d) Energy of interacting photon.

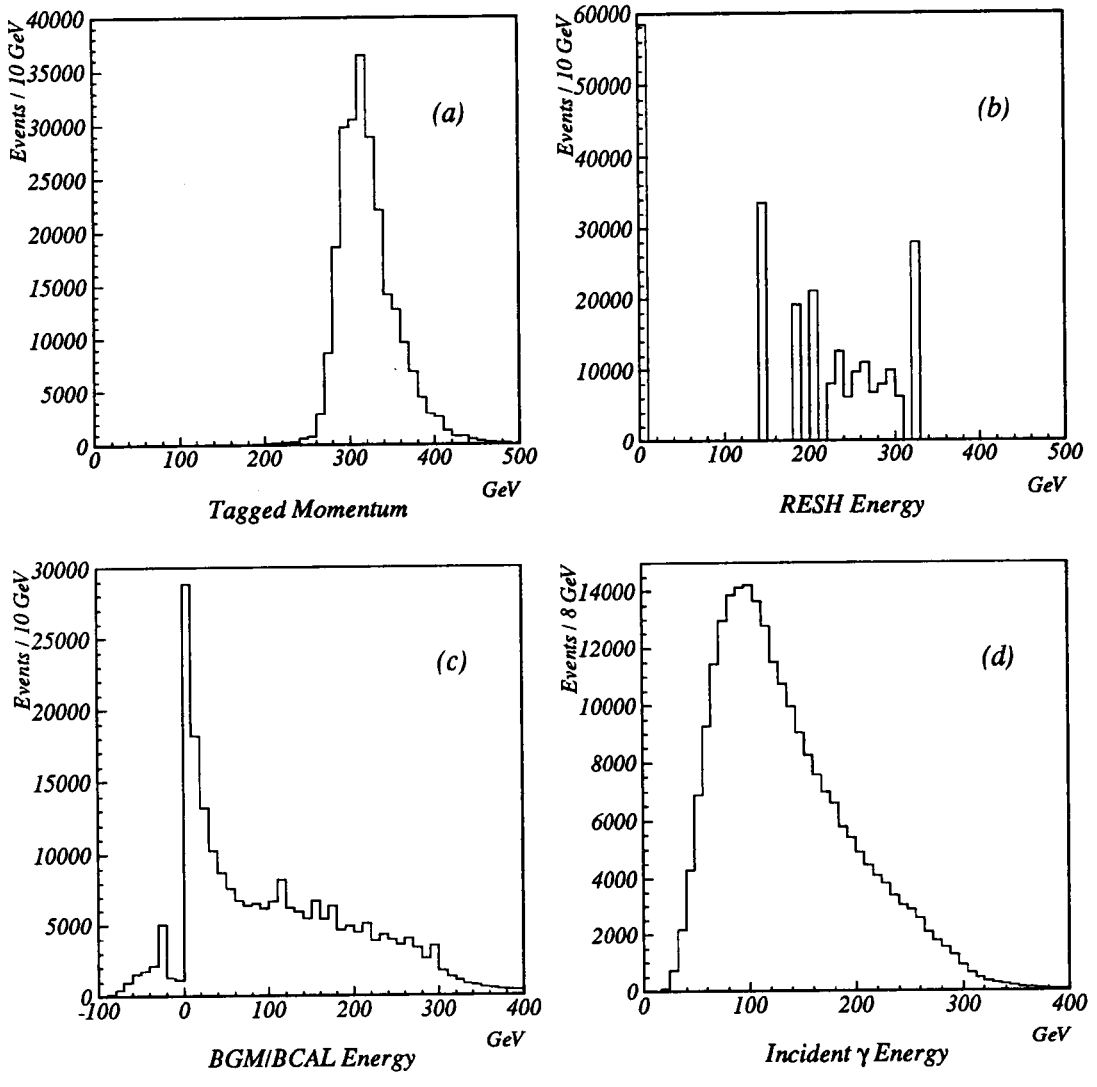

Figure 40: Beam characteristic plots of real data for the $K_S K\pi\pi$ channel: (a) The momentum of the tagged electron. (b) Energy recorded in the RESH. (c) Energy recorded in the BGM/BCAL. (d) Energy of interacting photon.

are almost identical to those in the $K_S K\pi\pi$ channel. The similarities between the real and Monte Carlo data suggest that the data are consistent with expectations for photoproduction, and are not due to contaminant particles in the beamline. The RESH energy appears different between the two sets of data because the RESH counters in the real data are digitized.

7.2.3 Track Momenta

The momentum spectrum of representative tracks in the laboratory frame are normalized and and plotted in Figure 41. The histograms represent Monte Carlo reconstructed data, and the dots represent the real data. Although small differences between the real and Monte Carlo data can be seen, the general tenor of these plots is the same for both data sets, and indicate no unexpected effects.

7.2.4 Angular Efficiencies

The angular efficiencies are determined in the helicity frame of the $f_1(1285)$ for the $K_S K\pi\pi$ channel. For the $KK\pi\pi\pi$ channel, angular efficiencies are determined in the helicity frame of the $\phi\eta$ resonance, the canonical frame of the ϕ and the helicity frame of the ϕ. These reference frames are purposely chosen because they do not directly depend of the direction of the beam, which is not always a well-known quantity in this experiment.

Mass cuts are taken to correspond to those used for the real data. The reconstruction efficiency is that determined with the inclusion of the Master Gate and Second Level triggers. The geometrical efficiency is the efficiency of the detector itself without the triggering system. The geometrical and reconstruction efficiencies are given in Figure 42 for the $K_S K\pi\pi$ channel and in Figure 43 for the $K^+K^-\pi^+\pi^-\pi^0$ channel.

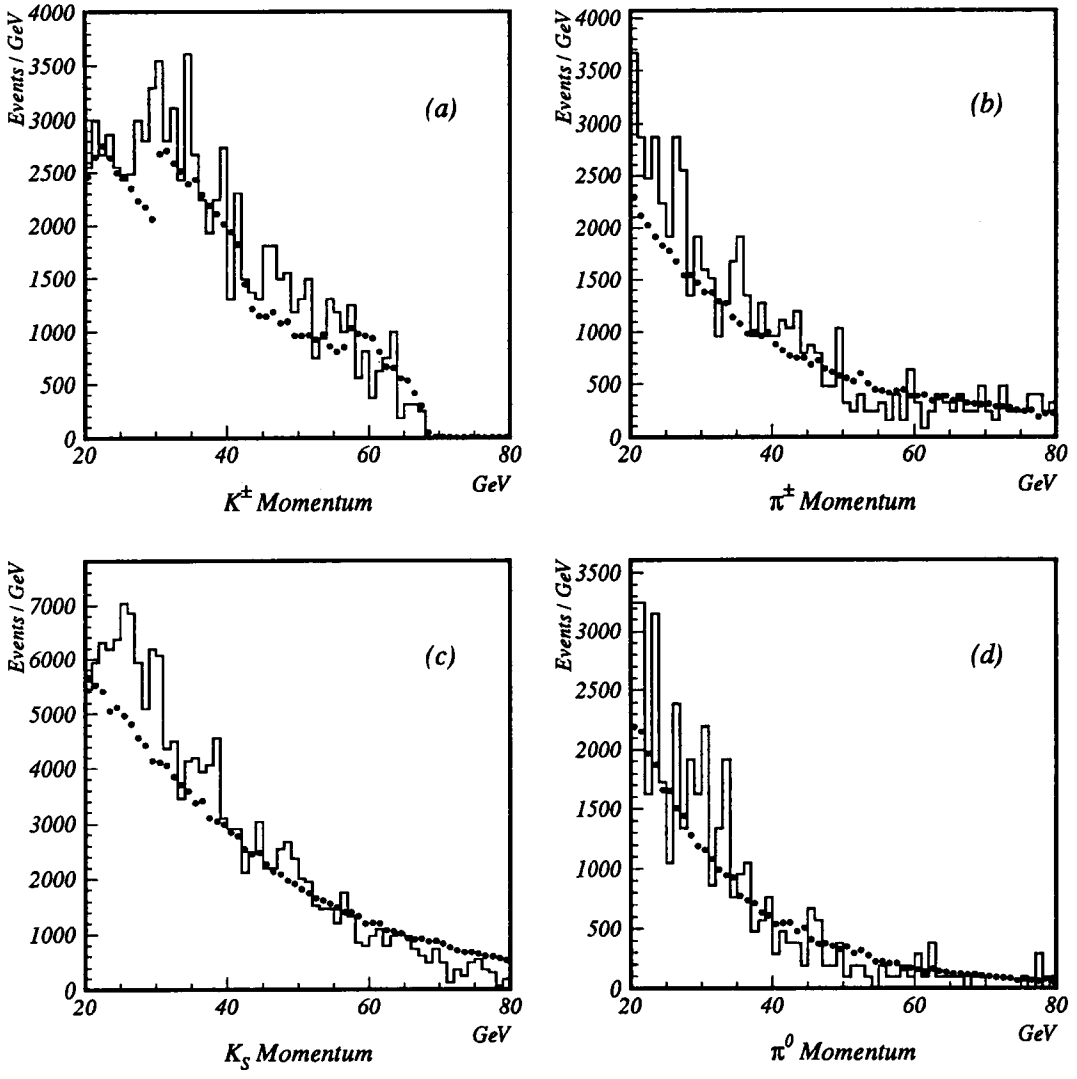

Figure 41: Normalized track momenta in the laboratory frame for the following tracks: (a) charged K's, (b) charged π's, (c) K_S's, and (d) π^0's. The lines represent the Monte Carlo data, and the dots represent the real data.

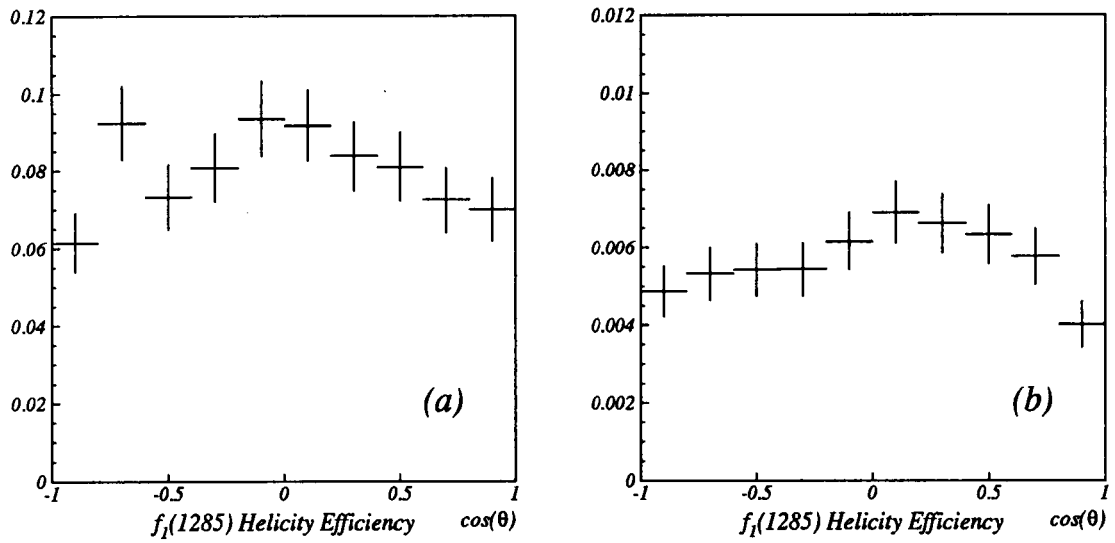

Figure 42: Efficiencies for the $f_1(1285)$ helicity angle (a) Geometrical efficiency and (b) Reconstruction efficiency.

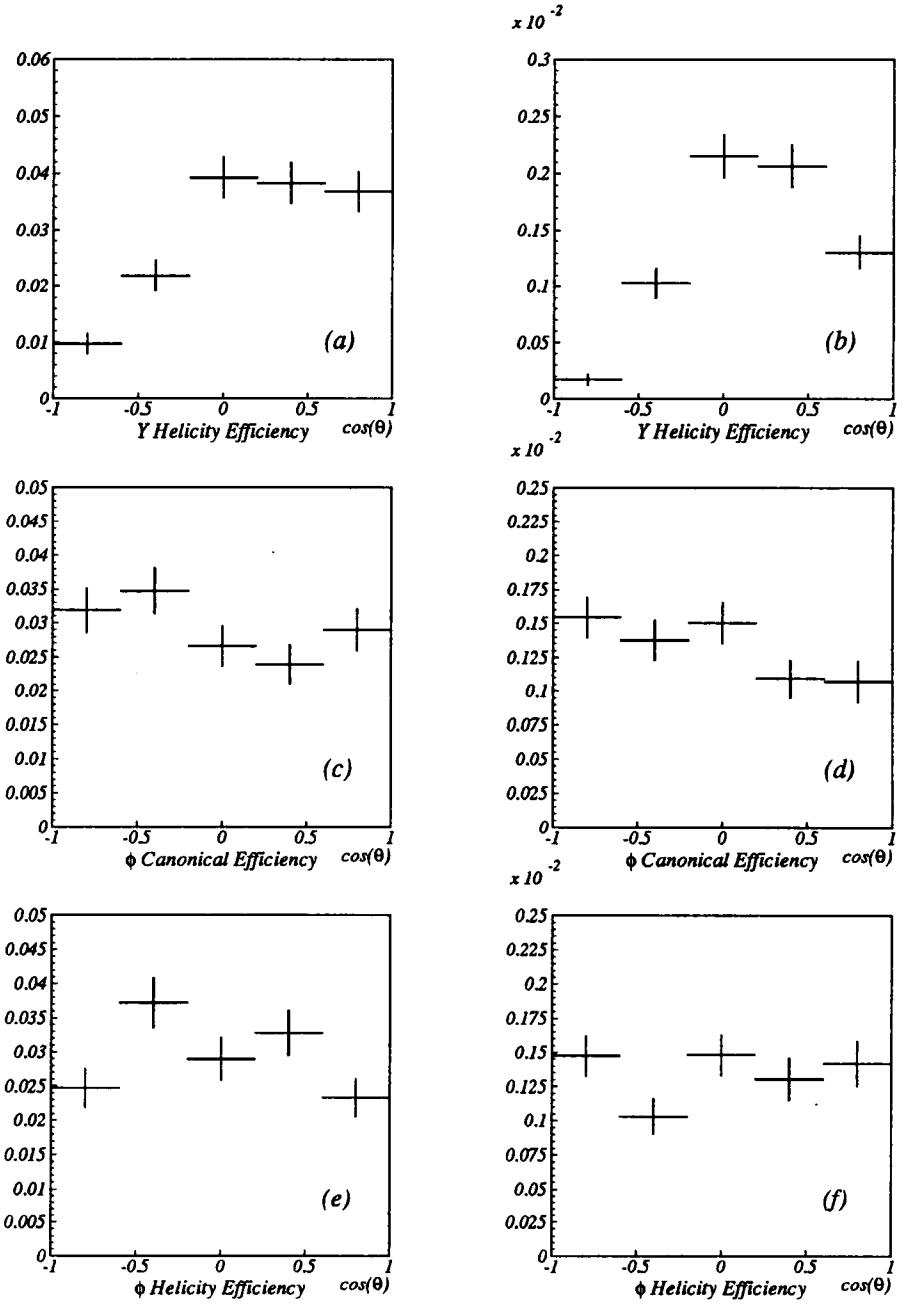

Figure 43: Angular efficiencies for the $\phi\eta$ resonance: (a) Geometrical efficiency for the helicity frame of the $\phi\eta$, (b) Reconstruction efficiency for the helicity frame of the $\phi\eta$, (c) Geometrical efficiency for the canonical frame of the ϕ, (d) Reconstruction efficiency for the canonical frame of the ϕ, (e) Geometrical efficiency for the helicity frame of the ϕ, and (f) Reconstruction efficiency for the helicity frame of the ϕ.

7.2.5 Reconstruction of π^0's

Unlike the K_S's, the π^0's are not reconstructed in the light quark skim. The user must reconstruct them from photon tracks in the IE. This is carried out in both the real and the Monte Carlo data, and the $\gamma\gamma$ mass spectrum of each is shown in Figure 44. The background in the real data is due to other processes involving photons.

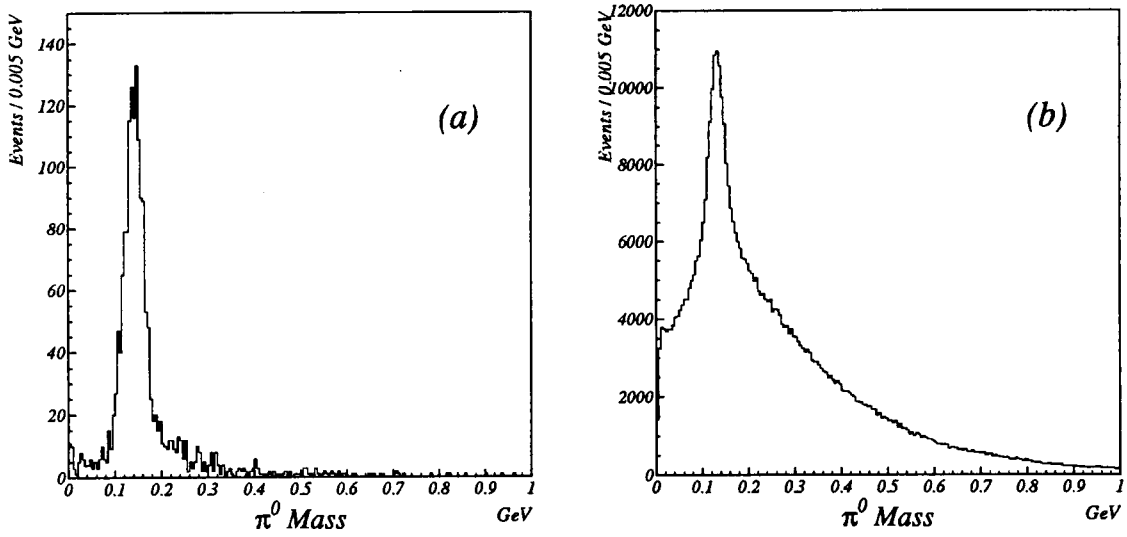

Figure 44: Reconstructed π^0's in (a) Monte Carlo data and (b) real data.

Chapter 8

Conclusions

Evidence has been presented for the existence of two possible hybrid mesons which have been predicted in the flux tube model. Since photoproduction has been suggested to be an ideal source of flux tube hybrid mesons, E687 is a suitable place to look for them.

In the $f_1(1285)\pi$ channel, which is one of the most experimentally accessible channels in the search for hybrid mesons as described by the flux tube model, there appears to be a resonance at a mass of 1748 ± 12 MeV and a width of 136 ± 30 MeV. An angular analysis reveals that this resonance is consistent with having $J^{PC} = 1^{-+}$. The $f_1(1285)\pi$ mass spectrum can be fit with a second peak of mass of approximately 1900 MeV, but the angular distribution was indistinguishable from that in the lower mass region, and hence was assumed to be part of the main resonance peak.

These findings are somewhat at variance with results reported by Lee *et. al.* [21]. While both analyses are in agreement that there is a $J^{PC} = 1^{-+}$ state in the mass region 1600-2200 GeV, the E687 data indicate a resonance with considerably smaller width. Furthermore the decay of the state observed in E687, in its helicity frame, contains no evidence for the presence of a state with $J^{PC} = 1^{++}$, which has been reported by Lee *et. al.*

The $\phi\eta$ channel is particularly interesting since this experiment represents the

largest sample of such events in the scientific literature except for J/ψ decays. In the E687 data there appears to be a clear $\phi\eta$ enhancement with a mass of 1914 ± 33 MeV and a width of 389 ± 115 MeV. A thorough angular analysis utilizing three different angles shows that the enhancement is consistent with only $J^{PC} = 1^{--}$. There is, thus, evidence for a new vector meson predicted by Close and Page [24], which decays to $\phi\eta$ and which occurs in a mass region predicted by Barnes, Close and Swanson [19]. Because of the non-exotic quantum numbers, this state cannot be unambiguously classified as a hybrid state, especially since the second radial excitation of the ϕ is expected in this mass region. However, strong correlations between theoretical predictions and experimental data suggest that the probability of this being a hybrid state must be considered.

Hybrid searches are continuing at UT. Currently E687 data are being analyzed in the $b_1(1235)\pi$ channel and other $f_1(1285)\pi$ channels.

BIBLIOGRAPHY

Bibliography

[1] T. H. Bauer *et. al.* Reviews of Modern Physics, **50**, 261 (1978).

[2] Schuler G. A. and T. Sjöstrand. Nuclear Physics B, **407**, 539 (1993).

[3] F. E. Close. *An Introduction to Quarks and Partons.* Harcourt Brace Jovanovich, (1979).

[4] T. Barnes. Hadron Physics Seminar. Oak Ridge National Laboratory, (1994-95).

[5] D. H. Perkins. *Introduction to High Energy Physics.* Addison-Wesley Publishing Company, Inc., (1987).

[6] R. Lacaze and H. Navelet. Nuclear Physics B, **186**, 247 (1981).

[7] G. S. Bali *et. al.* Physics Letters B, **378**, 378 (1993).

[8] Particle Data Group. Physical Review D, **50**, 1 (1994).

[9] F. deViron and J. Weyers. Nuclear Physics B, **185**, 391 (1981).

[10] T. Barnes, F. E. Close, and F. deViron. Nuclear Physics B, **224**, 241 (1983).

[11] M. Chanowitz and S. Sharpe. Nuclear Physics B, **224**, 211 (1983).

[12] I. I. Balitsky, D. I. Dyakonov and A. V. Yung. Zeitschrift für Physik C, **33**, 265 (1986).

[13] F. deViron and J. Govaerts. Physical Review Letters, **53**, 2207 (1984).

[14] D. Horn and J. Mandula. Physical Review D, **17**, 898 (1978).

[15] M. Tanimoto. Physical Review D, **27**, 2648 (1983).

[16] S. Ishida *et. al.* Physical Review D, **47**, 179 (1993).

[17] N. Isgur, R. Kokoski and J. Paton. Physical Review Letters, **54**, 869 (1985).

[18] S. Godfrey and N. Isgur. Physical Review D, **32**, 189 (1985).

[19] T. Barnes, F. E. Close and E. S. Swanson. Technical Report RAL-94-106, Rutherford Appleton Laboratory, January (1995).

[20] F. E. Close and P. R. Page. Technical Report RAL-94-122, Rutherford Appleton Laboratory, December (1994).

[21] J. H. Lee *et. al.* Physics Letters B, **323**, 227 (1994).

[22] T. Handler *et. al.* Submitted to Physical Review D, (1995).

[23] M. Atkinson *et. al.* Zeitschrift für Physik C, **34**, 157 (1987).

[24] F. E. Close and P. R. Page. Nuclear Physics B, **443**, 233 (1995).

[25] G. T. Condo *et. al.* Physical Review D, **43**, 2787 (1991).

[26] E. J. Mannel. *Decay Properites of the Charm Baryon* Λ_c^+. PhD thesis, University of Notre Dame, (1991).

[27] P. L. Frabetti *et. al.* Nuclear Instruments and Methods in Physics Research A, **329**, 62 (1993).

[28] P. L. Frabetti *et. al.* Nuclear Instruments and Methods in Physics Research A, **320**, 519 (1992).

[29] C. J. Kennedy. *A Measurement of Rare All-Charged Decays of the D^0 Meson.* PhD thesis, University of Notre Dame, (1993).

[30] G. R. Blackett. *Semi-inclusive Production of Light Mesons by High Energy Photoproduction.* PhD thesis, University of Tennessee, (1992).

[31] D. R. Claes. *Measurement of the $D^{*\pm}$ Photoproduction Cross Section.* PhD thesis, Northwestern University, (1991).

[32] G. R. Blackett. Private communication.

[33] URL http://www.hep.uiuc.edu/e687/images/c1.gif (1995).

[34] W. E. Johns. *Measurement of the Semileptonic Decay of the Neutral Charmed Meson $D^0 \to K^-\mu^+\nu_\mu$.* PhD thesis, University of Colorado, (1995).

[35] H. Méndez. *Measurement of the J/ψ Photoproduction Cross Section.* PhD thesis, Centro de Investigacion y de Estudios Avanzados del IPN, (1990).

[36] C. J. Dallapiccola. *Lifetime Measurements of the Charmed Strange Baryons Ξ_c^+ and Ξ_c^0.* PhD thesis, University of Colorado, (1993).

[37] S. Park *et. al.* Nuclear Instruments and Methods in Physics Research A, **289**, 496 (1990).

[38] S. Bianco *et. al.* Nuclear Instruments and Methods in Physics Research A, **305**, 48 (1991).

[39] M. Pisharody. *Light-Quark Meson Photoproduction at a Mean Energy of 120 GeV/c.* PhD thesis, University of Tennessee, (1993).

[40] D. Petravick *et. al. The PAN-DA Data Acquisition System.* Fermilab Computational Department Note, Fermi National Accelerator Laboratory.

[41] G. T. Condo *et. al.* Physical Review D, **48**, 3045 (1993).

[42] M. Nikolić. *Analysis of Scattering and Decay.* Gordon and Breach, (1968).

[43] B. Delcourt *et. al.* Physics Letters B, **113**, 93 (1982).

[44] T. Barnes. Private communication.

[45] K. L. Lingel. *Photoproduction of $D^{\pm}$ Mesons.* PhD thesis, University of Illinois, (1990).

Vita

KATHLEEN ANN DANYO was born on October 4, 1968, in Wyandotte, Michigan, a suburb of Detroit. She grew up in Riveriview, Michigan, and graduated from Riverview Community High School in 1986. The following September she matriculated at the University of Michigan-Dearborn. She graduated with a Bachelor's of Science Degree in Physics in May 1990. In August 1990 she entered graduate school as a teaching and research assistant at the University of Tennessee in Knoxville.